Enhanced penetration of pro-apoptotic and anti-angiogenic micellar nanoprobe in 3D multicellular spheroids for chemophototherapy

Anbu Mozhi, Vishnu Sunil, Wenbo Zhan, Pramila Baban Ghode, Nitish V. Thakor, Chi-Hwa Wang

PII: S0168-3659(20)30280-7

DOI: https://doi.org/10.1016/j.jconrel.2020.05.005

Reference: COREL 10312

To appear in: *Journal of Controlled Release*

Received date: 18 February 2020

Revised date: 27 April 2020

Accepted date: 4 May 2020

Please cite this article as: A. Mozhi, V. Sunil, W. Zhan, et al., Enhanced penetration of pro-apoptotic and anti-angiogenic micellar nanoprobe in 3D multicellular spheroids for chemophototherapy, *Journal of Controlled Release* (2019), https://doi.org/10.1016/j.jconrel.2020.05.005

Enhanced Penetration of Pro-Apoptotic and Anti-Angiogenic Micellar Nanoprobe in 3D Multicellular Spheroids for Chemophototherapy

Anbu Mozhi [1†], Vishnu Sunil[1†], Wenbo Zhan[2], Pramila Baban Ghode[3], Nitish V. Thakor[3,4], Chi-Hwa Wang[1*]

[1]Department of Chemical and Biomolecular Engineering, National University of Singapore, 4 Engineering Drive 4, Singapore 117585, Singapore

[2]School of Engineering, King's College, University of Aberdeen, Aberdeen AB24 3UE, UK

[3] Singapore Institute for Neurotechnology (SINAPSE), National University of Singapore, 28 Medical Drive, Singapore 117456, Singapore

[4]Department of Biomedical Engineering, Johns Hopkins School of Medicine, Baltimore, MD, United States

[†]These authors contributed equally to this work.

[*]Corresponding Author:

Email: chewch@nus.edu.sg (C.H. Wang)

Submitted to Journal of Controlled Release
April 2020

Abstract

Light irradiation is considered an ideal non-invasive stimulus that enables precise tumor treatment with flexible, facile, and spatiotemporal control. Photodynamic therapy (PDT) is an important clinically relevant therapeutic modality that has proven to compensate for the reduced therapeutic efficacy of conventional chemotherapy. However, oxygen consumption during PDT can result in an inadequate oxygen supply which reduces photodynamic efficacy. In our quest to circumvent the limitations of chemotherapy and photodynamic therapy, we have engineered a robust and smart "all-in-one" nanoparticle-based drug delivery system capable of overcoming biological barriers and leveraging on several synergistic cancer cell killing mechanisms. The fabricated Targeted Micellar Nanoprobe (TMNP) had exceptionally high encapsulation efficiencies of a hydrophobic drug simvastatin (SV) and a photosensitizer protoporphyrin IX (PpIX) due to the □-□ stacking of the aromatic groups of SV and PpIX and strong hydrophobic interactions with the alkyl chains of the carrier. In-vitro results demonstrated that TMNP exhibited excellent colloidal stability, biocompatibility and drug retaining capability in physiological condition. Under light irradiation, TMNP causes the accelerated generation of reactive oxygen species (ROS) which subsequently damages the mitochondria. On further evaluation of the mechanisms behind the superior anti-cancer effect of TMNP, we concluded that TMNP causes synergistic apoptosis and necrosis along with cell cycle arrest at the G1-S phase and elicits anti-angiogenic effects. Taking into consideration that these promising results on 2D monolayer cell cultures might not translate into similar results in animal models, we developed 3D multicellular tumour spheroids (MCs) as an intermediate step to bridge the gap between 2-D cell experiments and in-vivo studies. TMNPs showed enhanced penetration and growth inhibition on MCs. In addition, the modelling of the transport of TMNP in the tumour exhibited the improved effective delivery volume. Overall, TMNPs could potentially be used for image-guided delivery of the therapeutic payloads for precise cancer treatment.

Introduction

Currently, glioma patients have one or a combination of three treatment options: radiation therapy, chemotherapy or surgery [1]. Although surgical resection of the tumour is the preferred option, often it is not possible as the tumours cannot be separated from the surrounding tissue or is located near sensitive areas in the brain which makes surgery risky. Furthermore, in many cases, even after complete resection, the tumour recurs from the resection cavity margin [2]. Hence, chemotherapy is used an adjuvant treatment after surgery. However, the clinical efficacy of monotherapy using anti-cancer agents has been limited by its systemic toxicity, total dose restrictions, tumour heterogeneity, and inevitable drug resistance. To address this issue, combination therapies have been considered as a potential strategy for the treatment of gliomas [3].

Several studies have shown that drug delivery systems (DDSs) with two or more therapeutic components leveraging on different anti-tumour mechanisms provide a synergistic chemo-chemo, chemo-radio, chemo-photodynamic, chemo-thermal and chemo-siRNA effect, which results in enhanced cancer cell apoptosis, reduced tumour progression and minimal systemic toxicity. Among these, photodynamic therapy (PDT) has been extensively studied as it has several advantages over other treatment modalities such as non-invasiveness, fast cure process and superior spatiotemporal control [4, 5]. However, its therapeutic efficacy is hampered by PDT-mediated hypoxia developed during the treatment. To overcome this limitation, integration of PDT with chemotherapy would reduce the O_2 dependence for high therapeutic efficacy. Hence, the combination of photosensitizers with chemotherapeutic agents in a rationally designed "all-in-one" DDS to achieve chemophototherapy has attracted a lot of attention in clinical tumour treatment.

DDSs with innovative drug combinations have immense potential in countering drug resistance and in reducing tumour metastasis by inhibiting multiple tumour cell survival pathways [5]. Hu et al. validated that the combination of chlorin 6, doxorubicin (DOX) and manganese dioxide produced a synergistic anti-tumour effect by combined chemo-PDT along with generation of oxygen in an MCF-7 tumour-bearing mouse model [6]. Recently, Liu et al. developed a versatile metal-organic framework capable of selective cathepsin B responsive imaging and chemo-PDT therapy which exhibited superior treatment efficacy compared to individual therapies [7]. Lin's group developed nanoscale coordination polymers (NCPs) as a potential DDS to enable both chemotherapy and PDT in a single delivery system [8].

NCP@pyrolipid core–shell nanoparticle with high loading contents of the photosensitizer pyrolipid and oxaplatin was designed to synergistically induce cancer cell necrosis and apoptosis and provoke an immune response. Further treatment with PD-L1 checkpoint blockade therapy resulted in not only regression of primary tumours but also regression of the distant tumours by generating a systemic tumour-specific T-cell response [9].

2D cell cultures remain the most commonly used preliminary evaluation of the therapeutic efficacy of DDSs due to their reproducibility, simplicity and low cost [6, 7] . However, in most cases, promising results observed in these suboptimal 2-D monolayer cell culture systems result in misleading observations and conclusions and do not translate to similar results in animal models due to the absence of cell-cell or cell-extracellular matrix interactions [8-11]. Consequently, multitudes of ineffective therapeutics are tested on animals, resulting in overuse of animals in experimentation and increase in the overall time and cost of the development process [12-14]. Hence, we developed multicellular spheroids (MCs) as an intermediate step to bridge the gap between 2-D cell experiments and in-vivo studies. MCs closely mimic many of the therapeutically relevant pathophysiological characteristics of human solid tumours such as their structural organization, nutrient gradients, hypoxia and production of an extracellular matrix, which act as major barriers for penetration of the nanoparticles into solid tumours [15-17].

In this study, we aimed to exploit the advantages of the chemo-PDT by developing a dual-in-dual blood brain barrier (BBB) targeted nanoprobe for cancer cell imaging and a synergistic anti-tumour effect. 1,2-distearoyl-snglycero-3-phosphoethanolamine-N-[methoxy(polyethyleneglycol)-2000] (DSPE-PEG_{2000}) is an FDA approved material which shows excellent biodegradability and negligible toxicity upto 1000 µg/ml [18, 19]. The glutathione modified multifunctional DSPE-PEG_{2000} micellar nanoprobe (TMNP) was first encapsulated with an anti-cancer drug simvastatin (SV) and protoporphyrin IX (PpIX) as the signal and recognition moiety and photosensitizer. Simvastatin is a 3-hydroxy-3-methyl-glutaryl coenzyme A (HMGCoA) reductase inhibitor that reduces cholesterol synthesis by preventing the conversion of HMG-CoA to mevalonate and is currently used in the clinic to treat hypercholesterolemia and cardiovascular diseases in high-risk patients [20]. Interestingly, recent experimental studies and clinical trials have demonstrated that simvastatin can elicit an anti-tumour effect, improve clinical prognosis and significantly prolong the survival time of glioma patients by inducing cell cycle arrest and apoptosis and inhibiting angiogenesis [21-27]. Meanwhile, PpIX in when subjected to light of suitable

wavelength and in the presence of oxygen can directly kill tumour cells through apoptosis, necrosis and vascular damage [1, 28, 9].

Scheme 1 represents how the TMNPs cross the tightly regulated BBB via receptor mediated endocytosis and accumulate within the tumour tissue through the enhanced permeation and retention (EPR) effect. TMNP maintains structural integrity in the extracellular environment but intracellularly in an acidic environment releases SV and PpIX in a triggered fashion causing time- and site-specific cytotoxicity. Once the imaging of the cancer cells indicates adequate accumulation of the TMNPs, a 630 nm laser irradiation is used to activate the released PpIX to generate reactive oxygen species (ROS). Meanwhile, SV contributes to highly effective chemophototherapy involving synergistic apoptosis and

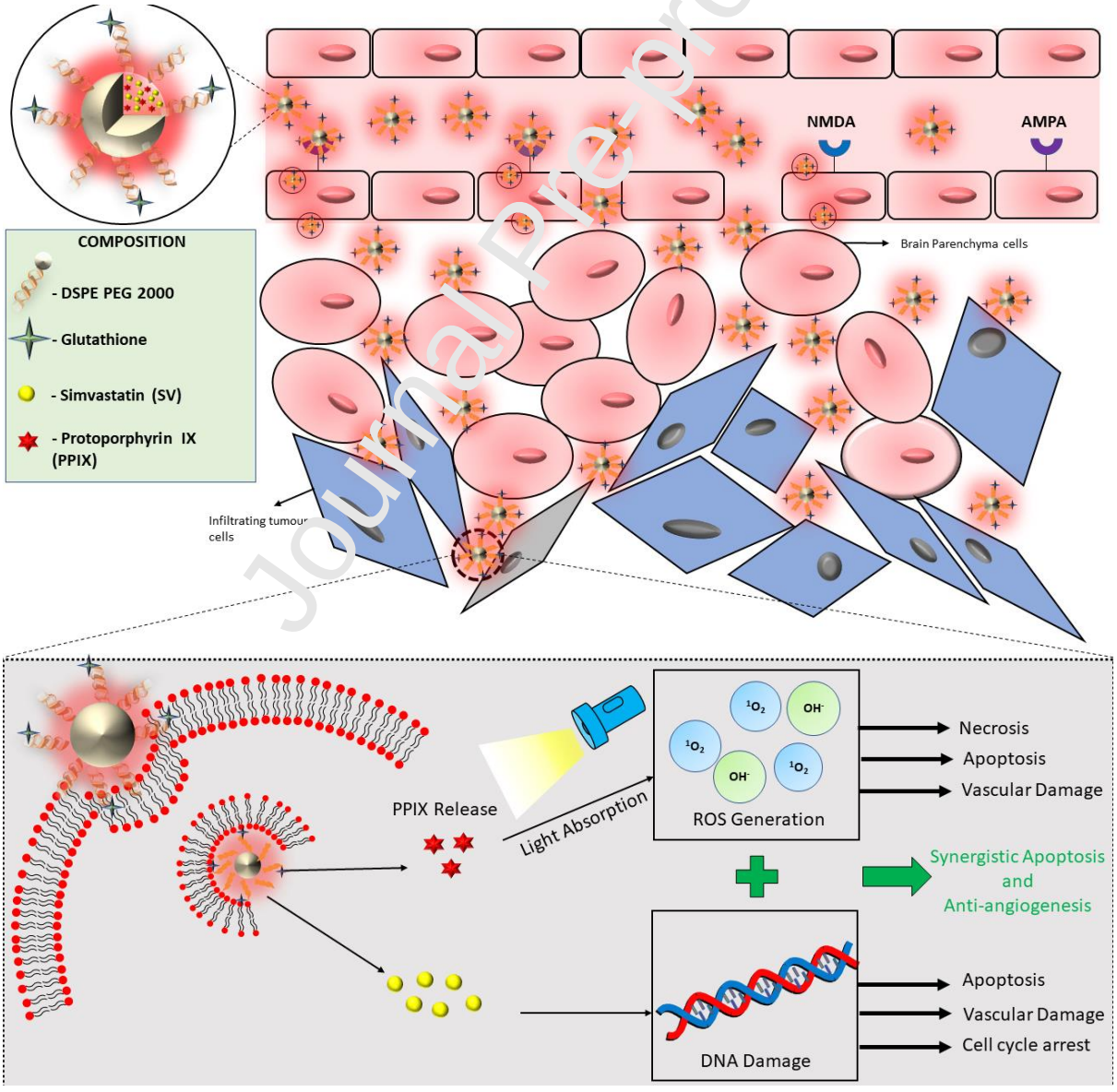

necrosis in addition to cell cycle arrest and vascular damage.

Scheme 1. Proposed cytotoxicity mechanism of TMNP. Schematic showing high concentration of TMNP surrounding the tumour by leveraging on receptor mediated endocytosis and leaky vasculature of the BBB.

2. Experimental Section

2.1 Materials

1,2-distearoyl-sn-glycero-3-phosphoethanolamine-N-[methoxy(polyethylene glycol)-2000] (DSPE-PEG_{2000}) and 1,2-distearoyl-sn-glycero-3-phosphoethanolamine-N-[maleimide (polyethylene glycol)-2000](DSPE-PEG_{2000}-MAL) were brought from Avanti Polar Lipids (USA). Reduced L-glutathione, simvastatin, 2',7'-dichlorodihydrofluorescin diacetate (DCFH-DA) and tetrahydrofuran (THF) were obtained from Sigma Aldrich (Singapore). CellTiter 96® AQueous One Solution Cell Proliferation Assay was purchased from Promega Corporation (USA). 4,6-Diamidino-2-phenylindole (DAPI), LysoTracker Green DND-26, JC-1 (5,5',6,6'-tetrachloro-1,1',3,3'-tetraethylbenzimidazolylcarbocyanine iodide) assay kit and Annexin V apoptosis detection kit were provided by Life Technologies. Dulbecco's Modified Eagle's Medium (DMEM), F-12K medium, fetal bovine serum (FBS), 0.25% trypsin-EDTA solutions, and penicillin-streptomycin were purchased from Gibco. The dialysis bags (MWCO = 1000Da) were from Spectrum Laboratories Inc. (USA).

2.2 Cell lines and cell culture conditions

C6 glioma cell line (rat), bEnd.3 cell (mouse), NIH/3T3 (mouse) and human umbilical vein endothelial cells (HUVEC) were brought from American Type Culture Collection (ATCC; Manassas, VA). C6, bEnd.3 and 3T3 cells were cultured in DMEM medium, supplemented with 10% FBS, 100 IU/ml penicillin and 100 mg/ml streptomycin. HUVEC cell line was cultured in F-12K medium. Cells were grown at 37 °C with 5% CO_2 conditions.

2.3 Synthesis and Characterization of Glutathione modified DSPE-PEG

DSPE-PEG-Glut was prepared via thiol maleimide "click" reaction of DSPE-PEG-MAL and L-reduced Glutathione [30]. Briefly, DSPE-PEG-MAL and L-reduced Glutathione (2:1, mol/mol) were dissolved in 4-(2-hydroxyethyl)-1-piperazineethanesulfonic acid (HEPES) and allowed to react overnight at room temperature. Subsequently, the solution was dialyzed (MWCO = 1000 Da) against distilled water at pH 7.4 for 24 hours and then lyophilized to

obtain DSPE-PEG-GLUT. The yield was observed to be 88%. The structure of DSPE-PEG-GLUT was confirmed using nuclear magnetic resonance (^{1}H NMR) and MALDI-TOF. ^{1}H NMR spectra of DSPE-PEG-MAL, L-reduced Glutathione and modified GLUT-DSPE-PEG were recorded on a nuclear magnetic resonance spectrometer (Ascend TM 600 MHZ,Bruker) were solubilized using deuterated DMSO as the solvent.

2.4 Preparation and Characterization of TMNP and MNP

A lipid film rehydration method was used to prepare TMNPs [31]. Briefly, 5 mg of DSPE-PEG, 5 mg of DSPE-PEG-GLUT, 0.8 mg SV and 0.4 mg PpIX were dissolved in 2 mL THF. Using a vacuum rotary evaporator, solvent was removed and a dry thin-film was obtained. At room temperature, the dried thin-film was hydrated with HEPES for 15 minutes. The unloaded SV and PpIX were removed using a 200 nm polycarbonate membrane (Millipore Co., Bedford, MA). MNPs were prepared using an identical procedure. The morphology of TMNP (SV and PpIX loaded Targeted Micellar Nanoprobe) was studied by transmission electron microscopy (TEM, JEM-2010F, JEOL, Japan) following negative staining with phosphotungstic acid. Particle size and zeta potential were recorded using a particle size analyzer (NanoBrook90 Plus, Brookhaven Instruments Co., USA) by dynamic light scattering (DLS) at a constant angle of 90°. A solution of TMNP (10 mg) dissolved in 1ml PBS (pH = 7.4). The concentration of SV and PpIX in the nanomicelles was determined using a UV-Vis spectrophotometer (Shimadzu UV-1700 spectrometer) at 205 nm and 405 nm respectively. Drug loading content (DLC) and drug loading efficiency (DLE) were calculated as follow:

$$DLC\% = \frac{Weight\ of\ loaded\ drug}{Weight\ of\ drug\ loaded\ micelles} \times 100\% \quad \text{..... (1)}$$

$$EE\% = \frac{Weight\ of\ loaded\ drug}{Weight\ of\ drug\ in\ feed} \times 100\% \quad \text{..... (2)}$$

2.5 In-Vitro Drug Release Study

In vitro release of SV and PpIX from TMNP was studied through the dialysis method under two different pH environments: sodium-acetate buffer (10 mM, pH 5.0) and PBS (10 mM, pH 7.4) [32]. Briefly, 1 ml of TMNP was transferred to a dialysis tube (MWCO 1000Da). The dialysis tube was dropped into the desired releasing media and shaken at 37 °C. At

different time points, 1 mL of the release medium was withdrawn and re-filled with 1 ml of fresh medium. The amount of released drugs was quantified by UV-Vis spectrophotometry.

2.6 Stability of Drug Loaded Micelles

The colloidal stability was studied by adding 100 µl of TMNP to 1 mL of water, HEPES buffer, and DMEM cell medium with 10% FBS and incubated at 37 °C, with gentle shaking at 50 rpm. The change in the micellar size at different intervals was studied using a 90Plus particle-size analyzer (Brookhaven Instruments Co., USA) instrument and the transmittance was measured at 750 nm by a microplate reader.

2.7 Evaluation of Hemolytic Activity

Freshly collected sheep Red blood cells (RBCs) were taken and washed thrice with sterile PBS (1500 g for 5 min). Serum was removed and the cells were mixed well in phosphate buffer. 500µL of six different sample concentrations (10, 20, 40, 80, 160, or 320 µg/mL) of TMNP in saline was mixed with 500 µL of RBC solution. The reaction mixture was left undisturbed for 2 h at 37 °C, and centrifuged again at 1500g for 5 min. The supernatant was carefully collected and the optical density (OD) was measured at 545 nm using a UV-Vis spectrophotometer by keeping blood/water mixture as a positive control (100% lysis) and blood/saline mixture as a negative control.

2.8 In-Vitro Cytotoxicity Studies

The cell toxicity of the free payloads and drug loaded micelles (SV concentration range 0.301 - 48.25 µg/ml) was studied using MTS assay. Free SV with/without light, free PpIX with/without light, and combination of free SV + free PpIX with/without light were also studied at concentrations similar to the co-loaded micelles. Briefly, C6 cells and 3T3 cells were grown into a 96-well plate at a density of 5×10^3 cells per well. The cells were then treated with different treatment groups for 24 h. After incubation, the culture media was removed and fresh medium was added to eliminate micelles which are not uptaken. The cells were irradiated with a 130 mW/cm^2 630-nm laser for 5 min and incubated for 4h. Cell viability was then evaluated by MTS assay in triplicate. After 2 h, the optical density was measured by a microplate reader (Tecan, Switzerland) at 490 nm.

For qualitative determination of live/dead cells, C6 cells were cultured at a density of 2×10^5 in each 35-mm glass-bottom dishes. After treatment with free drugs and co-loaded

micelles for 6 h, the PDT groups were irradiated with a 130 mW/cm^2 630-nm laser for 5 min. Later, the cells were rinsed and stained with calcein-AM and ethidium homodimer-1 for 20 min, washed three times with Dulbecco's phosphate-buffered saline (DPBS) and observed using Olympus inverted microscope.

2.9 In-Vitro BBB Penetration Study

An in-vitro BBB model was constructed using C6 and bEnd.3 cells using a non-contact co-culture transwell system as described previously [33]. Briefly, the upper chamber of transwells coated with 2% gelatin solution was used to culture bEnd.3 cells (1 x 10^4 cells/well) in DMEM containing 10% FBS for 7 days. Transepithelial electrical resistance (TEER) was used to measure the integrity of tight junction dynamics in the endothelial cell monolayer. Monolayers with TEER values higher than 300 Ω cm^2 were selected for experiments. C6 cells (4 x 10^4 cells/well) were seeded in the lower compartment of transwells. PpIX, MNP and TMNP (based on IC_{50} concentration) were added to the upper compartment to assess their penetration efficiency through the BBB. After 6 hours of incubation, the upper chamber was removed and the lower chamber was further incubated until 24 h. Confocal microscopy was used to observe the fluorescence intensity of the C6 cells.

2.10 Quantitative and Qualitative Intracellular Distribution of TMNP

Cellular uptake of the free drug and co-loaded micelles was investigated using confocal imaging. C6 cells were cultured into 35-mm glass-bottomed dishes at a density of 1.0 × 10^5 cells per well for 24 h. The cells were then incubated with 0.301 µg/ml of PpIX loaded targeted micelles in complete medium. Free PpIX and PpIX loaded micelles were also tested, in concentrations correspondent to the amounts loaded in PpIX targeted micelles. After incubation for 3 h and 6 h, cells were rinsed with DPBS and incubated with LysoTracker green for 20 min and rinsed with DPBS twice. The cells were fixed with 4% paraformaldehyde, washed, and stained with DAPI. The cells were washed again thrice with DPBS and observed by Confocal Laser Scanning Microscopy (CLSM).

Furthermore, the cell uptake was quantified by flow cytometry. At a density of 2 × 10^5 cells per well was grown in 6-well plates for 24 h. The cells were then treated with free PpIX, PpIX-loaded micelles and PpIX-loaded targeted micelles for 3 h. The drugs were removed and rinsed with DPBS for twice. The cells were then trypsinized, centrifuged and

replaced with 1 mL PBS to obtain a uniform suspension. The suspended cells were examined by a flow cytometer (Life Technologies).

2.11 Evaluation of Cellular Internalization Pathway

To evaluate the effect of temperature on the cell uptake, C6 cells (1.5×10^5) cultured in 8 well glass dishes were kept at 37 °C and 4 °C for 1 hour before adding the TMNPs (based on IC_{50} concentration). The cells were washed with DPBS thrice, fixed with 4% paraformaldehyde and stained with DAPI. Repeated washing with DPBS was done and CLSM was used to observe the resulting fluorescence. The mechanism of endocytosis of TMNPs in C6 cells was studied by pre-incubating the C6 cells with different endocytosis inhibitors such as dynasore (80mM), chlorpromazine (25mM), genistein (25mM) for 1 hour. Then, the cells were incubated with TMNP for 2 hour and washed with DPBS. The remaining procedures were followed as mentioned above.

2.12 Intracellular ROS Detection

ROS production was measured using DCFH-DA. C6 cells were cultured at a density of 2.5×10^5 cells per well in 35-mm glass-bottomed dishes for 24 h. The cells were then incubated with TMNP with SV concentration of 0.301µg/ml for 12 h. Free SV, free PpIX and MNP were also studied at concentrations similar to the co-loaded micelles. Drugs were removed and DCFH-DA (10 µM) in serum free medium was added and was left undisturbed for 1h. The cells treated with TMNP were irradiated with a 130 mW/cm^2 630-nm laser for 5 min. Control and treated groups were rinsed with DPBS thrice, and fixed with 4% paraformaldehyde for 20 min, stained with DAPI for 5 min. The cells were washed three times with DPBS and then imaged under CSLM.

2.13 Mitochondrial Membrane Potential Detection

Damaged mitochondrial membrane was detected using JC-1 dye. C6 cells were grown at 2.5×10^5 cells per well in 35-mm glass-bottomed dishes for 24 h. The cells were then incubated with TMNP with SV concentration of 0.301µg/ml for 12 h. Free SV, free PpIX and MNP were also tested in concentrations correspondent to the amounts loaded in TMNP. The cells treated with TMNP were irradiated with a 130 mW/cm^2 630-nm laser for 5 min and incubated further for 1 h. Positive control group was treated with CCCP for 5 min. Control and treated groups were rinsed with DPBS twice , stained with JC-1 (5 µg/mL) and

incubated for 20 min. The cells were fixed with 4% paraformaldehyde for 20 min; after being washed twice with DPBS, the cells were imaged by a confocal microscope.

2.14 Cell apoptosis study

The apoptosis cells percentage was quantified by Annexin V-FITC/PI detection kit. C6 cells were cultured in 6-well plates at a density of 2 $\times 10^5$ cells per well. The cells were treated with 0.301 μg/ml (SV concentration) of TMNP for 12 h. Free SV, free PpIX and MNP were also tested in concentrations similar to the amounts loaded in TMNP. The TMNP treated group was irradiated with a 130 mW/cm^2 630-nm laser for 5 min and incubated further for 12 h. The cells were then trypsinized, collected, centrifuged at 1500 rpm for 5 min and re-suspended in 200 μL of 1X annexin-binding buffer. Next, annexin V-FITC (5 μL) and PI (5 μL) were added to cell suspension tube and incubated at room temperature for 20 min protected from light. After incubation 1X annexin-binding buffer (400 μL) was added, mixed gently, placed on ice and then analyzed by flow cytometry.

2.15 Caspase enzymatic activity assay

Caspase enzymatic activity was quantified based on the instructions of the manufacturer for the caspase activity assay kit (Abcam, Singapore). The cells were treated with different treatment groups. After 12 h, the cells treated with Free PpIX, and TMNP were irradiated with a 130 mW/cm^2 630-nm laser for 5 min and incubated for 6 h. The cells were washed three times with DPBS. The C6 cells were then washed, trypsinized and centrifuged at 1500 rpm for 5 min at 4 °C. Supernatant was discarded and 50 μl cold lysis buffer was transferred into the tube to the lyse the cell pellets and incubated on ice for 1 h. Using the Bradford protein assay kit, the individual sample's total protein concentration was measured. 2× reaction buffer (50 μL) was added to the protein supernatant (50 μL) in each individual sample. Next, 10 μl caspase 9 and caspase 3 substrate was added and incubated at 37 °C for 1 h in dark. Lastly, each experimental sample were measured at 405 nm using a microplate reader.

2.16 Capillary tube formation assay

Growth factor reduced BD Matrigel (50μl) was transferred onto a 96 well plate and incubated at 37 °C for 30 min for gelation. Endothelial (HUVEC) cells suspended in serum-free F-12K medium was seeded on the Matrigel-coated plate at 20,000 cells per well. Cells were co-

incubated with serum-free medium containing various treatment groups as described in the cell apoptosis study. After 6 h of incubation, HUVECs formed tubes in the control group and the cells were carefully washed with DPBS without disrupting the tubules. The tubules were imaged using an inverted fluorescence microscope. Based on the number of branching points, the tube formation was quantified.

2.17 Cell cycle distribution

C6 cells were cultured in 6-well plates at a density 4×10^5 cells per well, incubated for 24 h, and treated with free SV, Free PpIX, MNP and TMNP (based on IC_{50} concentration) for 12 h. After PDT, the cells were incubated further 12 h. The cells were then harvested with trypsin, washed with cold DPBS, and fixed by pre-cold 70% ethanol for overnight at 4 °C. The cells were washed twice with DPBS centrifuged and treated with RNase A, and propidium iodide (PI) for 30 min at 37 °C in the dark condition. Finally, the stained cells were analyzed by a flow cytometer.

2.18 Growth Inhibition study in C6 Spheroids

C6 spheroids were cultured in ultra-low attachment 96 well round-bottom plates at a density of 2000 cells per well [34]. The plates were centrifuged at 1750 rpm for 10 min. After 2 days, the C6 spheroids were treated with TMNP with SV concentration of 0.301µg/ml in complete medium. Free SV, free PpIX, and MNP were also tested in equivalent SV concentrations. After 24 h, all the spheroids were washed thrice with complete DMEM and the TMNP treated group was irradiated with a 130 mW/cm^2 630-nm laser for 5 min. The medium was removed every alternate day and replaced with fresh medium. Spheroids were imaged using an inverted fluorescence microscope with a 10X objective lens (EVOS M7000). An automated image analysis macro developed for use with Image J (NIH, Bethesda, MD, Version 1.44 m) was used to measure the cross sectional area of the MCs, which in turn was used to determine the volume of the MCs across 7 days.

2.19 Evaluation of Penetration through C6 Spheroids

Three-Dimensional C6 spheroids were developed as mentioned in the growth inhibition study. The C6 spheroids were treated with 0.301 µg/ml of TMNP for 6 h. Free PpIX and PpIX loaded micelles were also tested, in concentrations correspondent to the amounts loaded in PpIX targeted micelles. The spheroids were then washed thrice with DBPS and fixed with

4% paraformaldehyde for 20 min. After washing thrice using DBPS, the spheroids were permeabilized with 1% Triton X-100 for 10 mins at room temperature. The spheroids were then dehydrated in an ascending series of methanol (25%, 50%, 75%, 100%) at 4°C for 15 mins each, and rehydrated in the same descending series and washed thrice with DBPS. Finally, the spheroids were stained with Phalloidin-iFluor 488 and DAPI for 1 h and washed thrice with DBPS before using CLSM for imaging.

2.20 Bio-TEM observation of C6 tumour spheroids

According to PpIX drug concentration, 3D tumour spheroids were incubated with TMNP at a concentration of 6.093 μg/mL for 12 h at 37 °C with 5% CO_2 atmosphere. The C6 tumour spheroids were harvested, washed with 1× DPBS (pH 7.4) and fixed with 2.5% glutaraldehyde for 3 h at 4 °C. The MCs were then washed DPBS twice, centrifuged at 1500 rpm for 10 minutes, and post-fixed with 1% osmium tetroxide in DPBS for 30 minutes. The cells were subsequently dehydrated with ethanol series from 25% to 100% and acetone for 10 minutes each, infiltrated and embedded in Araldite resin. The samples were trimmed on a microtome (Leica Ultracut UCT, Germany) and 100-nm thick sections were mounted on a TEM grid and stained with lead citrate for 8 minutes. The sections were observed with Tecnai Spirit G2 Transmission Electron Microscope (USA).

2.21 Modelling of TMNP transport in brain tumour

Brain tumour can briefly be divided into three compartments, including the extracellular space (ECS), cell membrane (CM) and intracellular space (ICS), respectively. TMNPs after penetrating BBB would experience multiple transport processes in these compartments, and finally release their therapeutic payloads in tumour cells as indicated in Scheme 1. The concentration of TMNP in ECS (C_{ECS}) depends on the diffusive and convective transport with interstitial fluid flow and dynamic association with receptors on CM, governed by

$$\frac{dC_{ECS}}{dt} = D_{ECS}\nabla^2 C_{ECS} - \nabla\cdot(\mathbf{v}C_{ECS}) - k_a C_{ECS} + k_i \quad \text{.....(3)}$$

where $\mathbf{v}$ is the interstitial fluid velocity. D_{ECS} stands for the TMNP diffusivity in tumour ECS. k_a and k_i are the rates of TMNP association and dissociation with receptors, respectively. As the associated TMNP on CM can be taken-up by tumour cells, this TMNP concentration (C_{CM}) is calculated by

$$\frac{dC_{CM}}{dt} = k_a C_{ECS} - k_i C_{CM} - k_e C_{CM} + k_c C_{ICS} \quad \text{.....(4)}$$

where k_e and k_c are the rates of cell endocytosis and cell recycling, respectively. Moreover, taking into account of the intracellular drug release, the TMNP concentration in tumour cells (C_{ICS}) is given by

$$\frac{dC_{ICS}}{dt} = k_e C_{CM} - k_c C_{ICS} - k_{rel} C_{ICS} \quad \text{.....(5)}$$

in which k_{rel} is the drug release rate.

The flux of TMNP penetrating BBB (J_{CB}) can be expressed as

$$J_{CB} = P_{CB}(C_{IVS} - C_{ECS}) \quad \text{.....(6)}$$

where P_{CB} is the transvascular permeability, C_{IVS} refers to the concentration in blood. The **Eq.(5)** is applied as the boundary condition to count the amount of TMNPs entering the tumour from blood.

The interstitial fluid velocity was found in the scale of 1.0E-7 m/s in brain [35]. The values of rest model parameters are summarised in **Table 1.** Transient simulations are performed until the dynamic equilibrium established between the source term and sink term, which refer to the TMNP gain from blood and the intracellular release, respectively.

Table 1. Model parameters

Parameter	MNP	TMNP	Source
Transvascular permeability * (m/s)	1.0E-9	4.5E-9	[36, 37]
Diffusivity in ECS ¥ (m^2/s)	1.13E-11	1.13E-11	[37, 38]
Association rate with receptor on CM (min^{-1})	1.0E-1	1.0E-1	[39, 40]
Dissociation rate with receptor on CM (min^{-1})	1.0E-2	1.0E-2	[39, 40]
Endocytosis rate (min^{-1})	1.0E-1	1.0E-1	[39, 40]
Recycling rate (min^{-1})	1.0E-3	1.0E-3	[39, 40]
Release rate † (min^{-1})	1.2E-1	1.2E-1	[41]

* The transvascular permeability of TMNP is estimated 4.5 times higher based on Figure 3(c).

¥ The diffusivity is estimated based on the cited references and the TMNP and MNP size of 80 nm.

† Release rate is derived from results of pH=5.0 shown in Figure 1(f), with the lower value adopted.

2.22 Statistical analysis

The quantitative data collected were expressed as mean ± S.D. Statistical significance was analyzed using three-sample Student's test. All experiments were performed in triplicates, $P < 0.05$ was considered statistically significant.

3. Results and Discussion

3.1 Construction and Characterization of the theranostic nanoprobe

The hydrophobic core inside the micelle formed by DSPE provides a stable environment for encapsulating both SV and PPIX, while hydrophilic PEG on the surface increases the hydrophilicity of the whole drug-loaded micelle. Furthermore, hydrophilic PEG chains provide stealth properties and steric stabilization, thereby increasing the in-vivo circulation

time of the micelles. The conjugation of an endogenous tripeptide, glutathione to DSPE-PEG-MAL can be rationalized due to the overexpression of sodium-dependent glutamate receptors such as AMPA and NPSH present on the BBB and glioma cells [42-47]. Average molecular masses of DSPE-PEG-MAL and DSPE-PEG-GLUT which were measured by performing matrix-assisted laser desorption/ionization time-of-flight mass spectrometry (MALDI–TOF MS), were 2941 and 3248 Da, respectively (Figure 1a), indicating successful conjugation of glutathione onto DSPE-PEG-MAL. The molecular structure of the prepared DSPE-PEG-MAL was determined using the ^{1}H NMR spectra (Figure S1). The DSPE-PEG-GLUT spectrum clearly shows the PEG resonance peak at □3.5 ppm and was unaffected by the conjugation with L-reduced Glutathione. The resonance peak at □ 6.92 ppm represents the terminal Mal group of DSPE-PEG-MAL. However, in the spectrum of DSPE-PEG-GLUT, the MAL peak disappeared, suggesting that the Mal groups of DSPE-PEG-MAL had reacted with the thiol groups of L-reduced Glutathione. This data further corroborates the successful conjugation of Glutathione with the DSPE-PEG_{2000}-MAL. Using NMR, the degree of substitution was calculated to be ~71.78%.

By varying the weight ratios of SV to PpIX to DSPE-PEG_{2000} (m_{SV}: m_{PPIX}: $m_{DSPE\text{-}PEG2000}$) micellar nanoprobes were formulated (Table S1). The formulated nanoprobes were studied to determine their particle size, polydispersity indices (PDI), surface charge, encapsulation efficiencies and drug loading content. Initially, by increasing the mSV: mDSPE-PEG_{2000} ratio, the diameter of the nanoprobes decreased, while the drug loading efficiency increased (Table S1). This may be due to strong hydrophobic interactions between the phenyl groups of SV and the alkyl groups of DSPE-PEG_{2000} [48]. However, when PpIX is incorporated into the micellar core along with SV, the size increases by ~5 times. This indicates that co-loading of PpIX and SV in the hydrophobic core increases the volume of micelles. It was interesting to note that as the SV content increases in the nanoprobe, the encapsulation efficiency of PpIX also increases, thereby facilitating high loading content of both SV and PpIX. This correlation is due to the □-□ stacking of the aromatic groups of SV and PpIX [49-51]. Modifying the MNPs with glutathione resulted in a slightly bigger TMNP (Figure 1b). The morphologies of TMNP were examined by TEM. The TMNP had a uniform particle size of ~80 nm with spherical morphology (Figure 1b inset). The TEM images displayed a smaller particle size compared to the particle size determined by DLS, which can be attributed to the stretching property of the hydrophilic PEG terminal and swelling of the hydrophobic micellar cores in aqueous medium. It was also observed that the surface charge

of the micelles became more negative when PpIX and glutathione were incorporated into the formulation (Figure 1c). The increase in negative charge of TMNP compared to SVLM and MNP is due to the negatively charged carboxyl groups in Glutathione [52]. TMNP also showed favorable structural stability in physiological environment as there was negligible change in the particle size and PDI when the micelles where incubated in DMEM cell medium (Figure S2). TMNPs at different concentrations showed no visible hemolytic effects indicating excellent hemocompatibility (Figure S3).

The absorption properties of PpIX and SV were still intact after being loaded onto the PE-PEG micelles as confirmed by UV/Vis spectroscopy (Figure 1d). TMNP showed a characteristic sharp Soret band at 405 nm and the well-known "stairs" in the 450-630 nm region (Q band of PpIX) along with the absorption maxima of SV at 205 and 237 nm. It is interesting to note that the wavelength of maximum absorbance (λmax) was independent on the loading percentage of PpIX and SV. PpIX existed as a monomer inside the hydrophobic micellar core as indicated by the Soret band at 405 nm and this was proven by the absence of peak shift in the fluorescence spectrum. This lack of aggregation increases the efficacy of PDT as aggregated porphyrins usually have a low photoactivity [53]. After encapsulation of PpIX, the TMNPs turn out to be fluorescent. However, at the same loaded concentration the fluorescence intensity of TMNP was comparatively lower than the free PpIX. As PpIX was loaded onto the micelles, the □-□ stacking of their aromatic group with those of SV might have caused the fluorescence quenching of 2.1 times over free PpIX, as measured by the change in fluorescence intensity (Figure 1e).

Table 2. Summary of formulations (SVLM – Simvastatin loaded micelles, MNP – Micellar Nanoprobe and TMNP – Targeted Micellar Nanoprobe)

Formulation	Size (nm)	EE% (SV)	DLC% (SV)	EE% (PpIX)	DLC% (PpIX)
SVLM	24.82 ± 1.5	95.36 ± 0.2	7.62 ± 0.02	-	-
MNP	100 ± 1	96.51 ± 1	7.72 ± 0.08	97.54 ± 0.5	3.90 ± 0.02
TMNP	112 ± 3.4	96.23 ± 0.53	7.69 ± 0.05	96.84 ± 0.8	3.87 ± 0.03

3.2 In-Vitro Passive Release Characteristics of TMNP

The passive release of PpIX and SV from TMNP at different pH values was examined using a dialysis method. The release of PpIX and SV from TMNP is plotted in accordance with time (Figure 1f). At pH 7.4, SV and PpIX exhibited a first-order burst release in the first 7.5 hours, before the release rate gradually slowed and stopped after 33 hours. Whereas, at a mildly acidic pH 5, the burst release is more pronounced. The final amount of SV and PpIX passively released after 33 hours increased from 9% and 7% (pH 7.4) to 82% and 77% (pH 5) respectively. This pH dependent release pattern suggests that the micelles remain stable at the blood and physiological pH level, whereas in the acidic microenvironment of the tumour cells, the micelles disassemble and release the encapsulated agents.

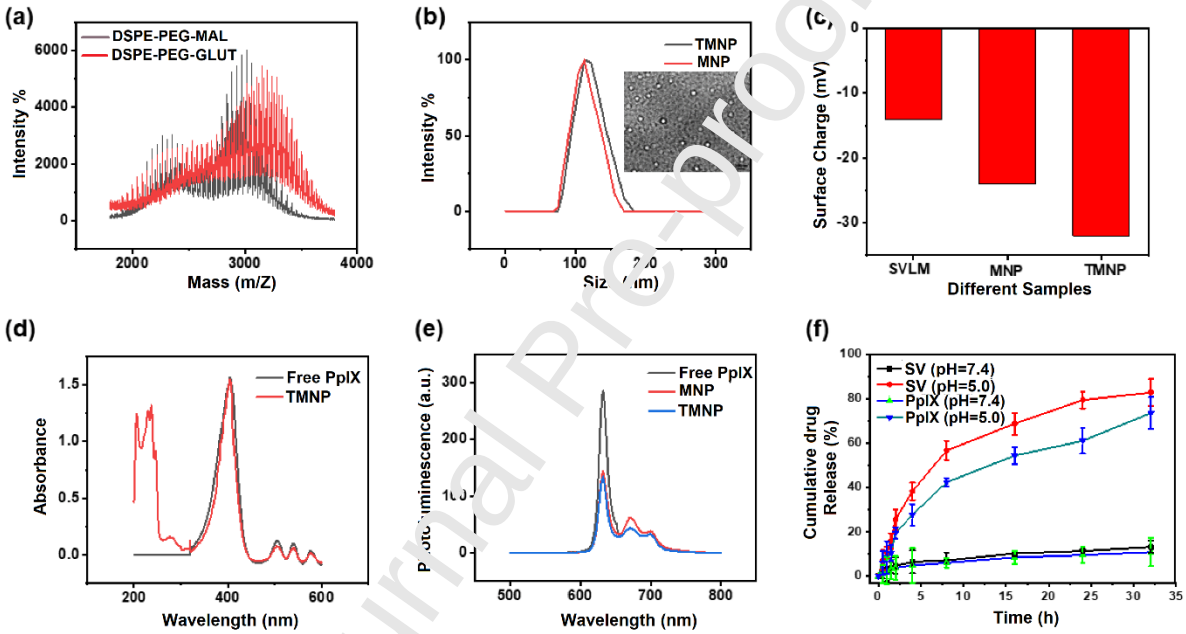

Figure 1. Characterization. a) MALDI-TOF spectra of DSPE-PEG-MAL (black) and DSPE-PEG-GLUT (red). b) Hydrodynamic diameter (DH) histogram distribution profile of TMNP (black) and MNP (red), (inset) TEM image of TMNP, Scale bar 200 nm. c) Zeta potential of SVLM, MNP and TMNP. d) Absorbance spectra of free PpIX (black) and TMNP (red). e) Fluorescence emission spectra after excitation at 405 nm of free PpIX (black) and TMNP (red). f) Release of SV and PpIX from TMNP over time in of different pH solutions. (SVLM = Simvastatin loaded micelles; MNP = SV and PpIX loaded Micellar nanoprobe; TMNP = SV and PpIX loaded Targeted Micellar nanoprobe).

3.3 Cytotoxicity of TMNP via combined chemotherapy and PDT

The effect of drug concentration, irradiation time, power density as well as the presence or absence of light exposure on C6 cell line was evaluated. The cytotoxicity of different drug formulations with/without irradiation was investigated on C6 and 3T3 cell lines via standard

MTS assays. For in vitro therapeutic experiments, each group exhibited a concentration-dependent cytotoxicity (Figure 2a, b, c, d). It should be noted that an enhanced therapeutic effect was observed in the TMNP + Light group, which might be ascribed to the synergistic effects of chemotherapy and PDT. Without PDT, PpIX showed an excellent cytocompatibility on C6 and bend.3 cells. Although, the brain tumour model used in this study (C6 cells) is usually associated with a relatively leaky BBB [54], the efficacy of MNP on C6 brain tumour growth and survival was small. However, the therapeutic efficacy of TMNP at a similar dose was significantly higher. Interestingly, □90% of 3T3 cells are viable after treatment with TMNP at a SV concentration 6.031 µg/mL, which decreases to ~80% even after light irradiation at 130mW/cm^2 for 5 minutes (Figure 2a). Meanwhile, at the same SV concentration TMNP + light reduces the cell viability to ~40% (Figure 2d). This indicates that glutathione as a targeting ligand does have added therapeutic value.

A live cell staining assay was used to visualize the enhanced tumour cell-killing efficacy of TMNP. As seen in Figure 2e, C6 cells treated with PBS (control) displayed vivid green fluorescence. While the C6 cells that received free SV, treatment showed moderate cell death, cells treated with free PpIX showed almost no toxicity as expected. Compared to monotherapy, MNP and TMNP showed significant cell death. However, when cells treated with TMNP subjected to light, almost all the cells were killed due to the synergistic effect of activated PpIX and SV.

The in vitro cytotoxicity studies clearly proved that sole modal therapy is not the perfect treatment option due to dropping O_2 content in cancer cells during PDT and significant toxicity to healthy brain cells during chemotherapy. Thus, a combined chemophototherapy should be applied to ensure the desired outcome. Hence, we further studied the tumour killing mechanisms behind the exhibited cytotoxicity.

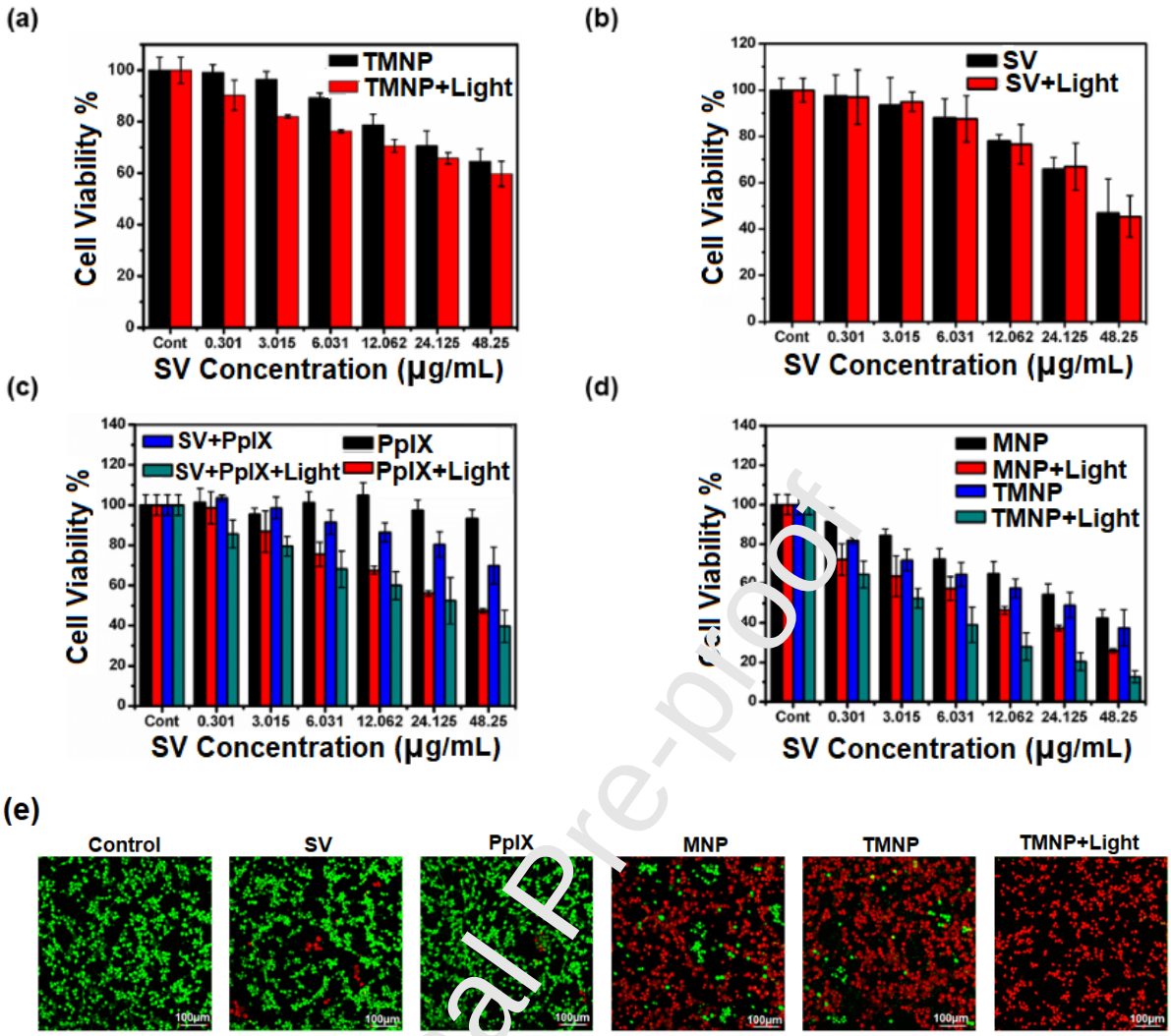

Figure 2. In vitro cancer cell-killing efficacy of TMNP. Cell viability after dosing a) 3T3 and b, c, and d) C6 cells with varying concentrations of treatment groups with/without irradiation (635 nm laser at 130 mW/cm2 for 5 minutes) in a medium supplemented with serum for 24 hours. (n = 3), e) CLSM photographs of C6 cells received different treatments. Calcein AM and ethidium homodimer-1 staining was performed for live cells (green) and dead cells (red) respectively. Scale bar, 100 μm.

3.4 In-Vitro BBB Penetration Study

Blood brain barrier permeability is the primary limiting factor for the penetration and distribution of therapeutics from blood to brain. Having evaluated the stability and safety of the prepared micelles, we then investigated its BBB-penetrating efficiency. Several studies have reported that monolayer bEnd.3 cells express appropriate tight junction proteins and transporters and closely mimics the primary cultures of BBB endothelial cells [55, 56]. Figure 3 shows a schematic illustration of the constructed BBB model. FITC-dextran (4kDa), Alexa 555 cadaverine and FITC-dextran (70kDa) were used to validate the BBB mimics.

While Alexa 555 cadaverine and FITC-dextran (4kDa) passed through the BBB, FITC-dextran (70kDa) could not pass through the BBB. As seen in Figure 3, only a limited amount of PpIX passed through the BBB monolayer and accumulated in the C6 cells cultured in the lower chamber of the setup. In contrast, the fluorescence intensity of TMNP in the cytoplasm of the C6 cells was significantly higher than that of PpIX and MNP. This results further proves the ability of Glutathione to facilitate the transport of therapeutic agents across the BBB as reported in previous studies [46, 57-59].

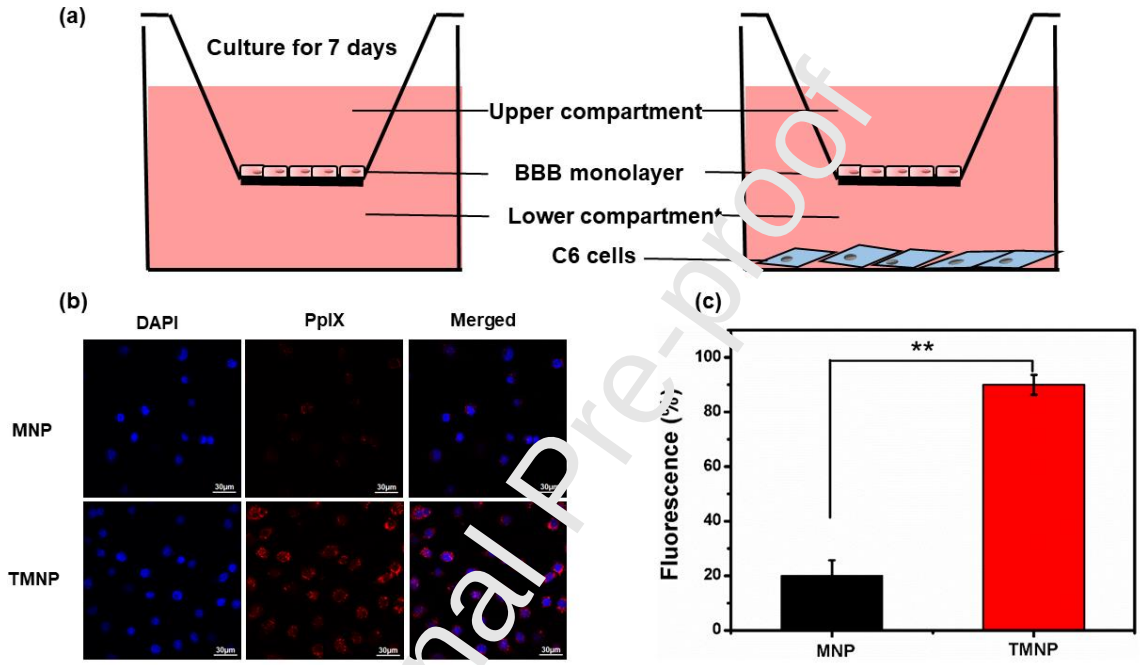

Figure 3. In-vitro BBB penetration study. a) Schematic representation of the in-vitro BBB model. b) CLSM photographs of MNP and TMNP in C6 cells after transporting across the BBB model. c) Fluorescent statistic of C6 cell uptake efficiency of MNP and TMNP after transporting across the BBB model. Scale bar, 20 μm **P < 0.01 and ***P < 0.001.

3.5 Cell Imaging and Colocalization Assays of TMNP

For in-situ imaging, C6 cells were treated with Free PpIX, MNP and TMNP for 3 and 6 hours. We used both flow cytometry and CLSM images to show that the infiltration of TMNP into the C6 cells was both time and dose-dependent. As shown in Figure 4a, 4b TMNP is internalized by cells in its intact form and its lipid layer gradually disassociates from the aqueous hydrophobic core and is distributed in the cytoplasm or translocated to cell membrane. A significantly higher PpIX fluorescence was detected when the cells were treated with TMNP when compared to the delivery of the same PpIX concentration in MNP

and its free form, under the same excitation and acquisition parameters. The higher PpIX uptake with TMNP might be elucidated by the endocytosis internalization pathway compared to free PpIX molecules which have limited receptor-mediated endocytosis. CLSM images indicated that the fluorescence of PpIX in TMNP treated cells was located predominantly in the lysosome. The group treated with TMNP had the highest mean fluorescence intensity which was almost 4-fold higher and 2-fold higher than free PpIX and MNP respectively.

It should be noted that despite the quenching of PpIX by SV, both MNP and TMNP show a higher fluorescence intensity compared to free PpIX. Hence, the enhancement of PpIX and SV uptake with TMNP would be even more significant if the quenching effect is taken into consideration. As shown in Figure 1d, e, the quenching effect of SV on PpIX is ~ 2.1 times. Hence at 6 hours, the corrected fluorescence intensity level of TMNP and MNP compared to free PpIX would be ~ 8 times and ~4 times higher respectively.

Furthermore, the flow cytometry result (Figure 4c) and its mean fluorescence intensity result (Figure 4d) indicates that after surface modification with GSH on to the micellar nanoprobe, the cellular uptake of TMNP has greatly enhanced compared to that of free PpIX and MNP. These results suggested that the uptake of nanoprobes by the C6 cells are through receptor mediated endocytosis.

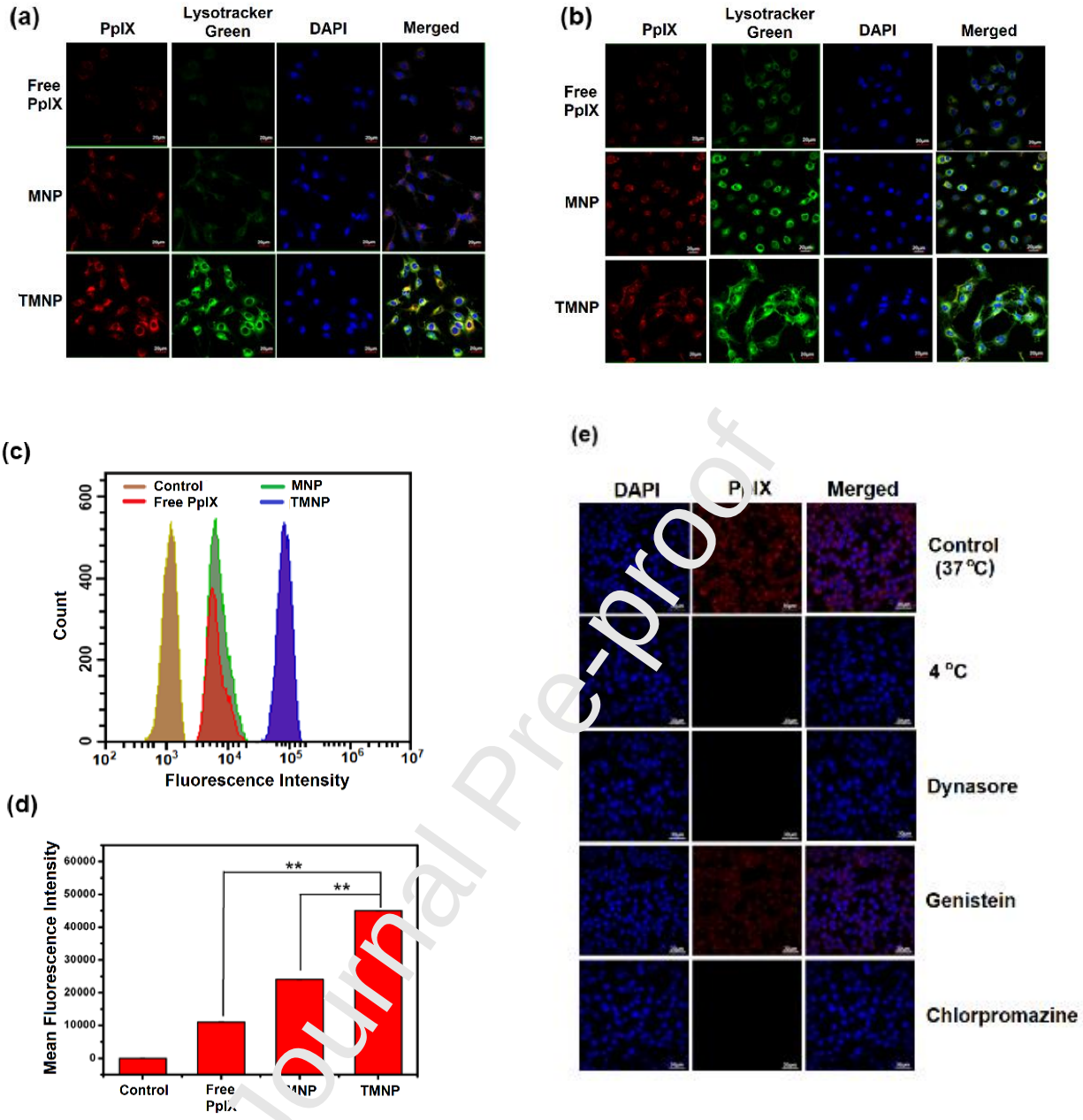

Figure 4. Cellular uptake dynamics. CLSM images showing the internalization and intracellular distribution of Free PpIX, MNP and TMNP in C6 cells at a) 3 hours and b) 6 hours. c) Quantitative analysis of the Free PpIX, MNP and TMNP uptake by C6 cells using flow cytometry. d) Mean fluorescence intensity of C6 cells after treatment with Free PpIX, MNP and TMNP. e) Cell uptake of TMNP after incubation at 37 °C and 4 °C and after preincubation with inhibitors of dynamin (dynasore) or caveolin (genistein) or clathrin (chlorpromazine). Scale bar, 20 μm. **P < 0.01 and ***P < 0.001.

2.6 Evaluation of Cellular Internalization Pathway

To determine if the micellar uptake by C6 cells is a temperature dependent process, we performed uptake experiments at 37 °C and 4 °C. As seen in Figure 4e, the fluorescence

microscopy signal of TMNP observed at 37 °C was lost when cells were incubated at 4 °C. This indicates that the micellar uptake is an active temperature dependent process.

Furthermore, to understand the early steps in the process of micellar uptake taking place in C6 cells in more detail, we pre-incubated the C6 cells with different selective inhibitors before treatment with TMNP. Dynamin is an important mediator in the scission of endocytotic vesicles from the cell membrane, which is a crucial step in the internalization of extracellular substances. Dynasore which is a selective inhibitor of dynamin significantly reduced the cellular uptake of TMNPs. Dynamin is associated with various endocytotic pathways such as clathrin- or caveolin- dependent routes [60, 61]. To investigate the exact endocytotic route, we used genistein and chlorpromazine to block caveolin- and clathrin-mediated endocytosis, respectively. The micellar uptake had negligible change with increasing concentrations of genistein. However, chlorpromazine exhibited a dose-dependent inhibitor effect on the cellular uptake of TMNP (Figure 4e). This result confirms that TMNP is internalized via receptor-mediated endocytosis.

3.7 Intracellular Photodynamic Behaviour

Upon specifically uptaken by the tumour cells, the intracellular photoactivity of TMNP was

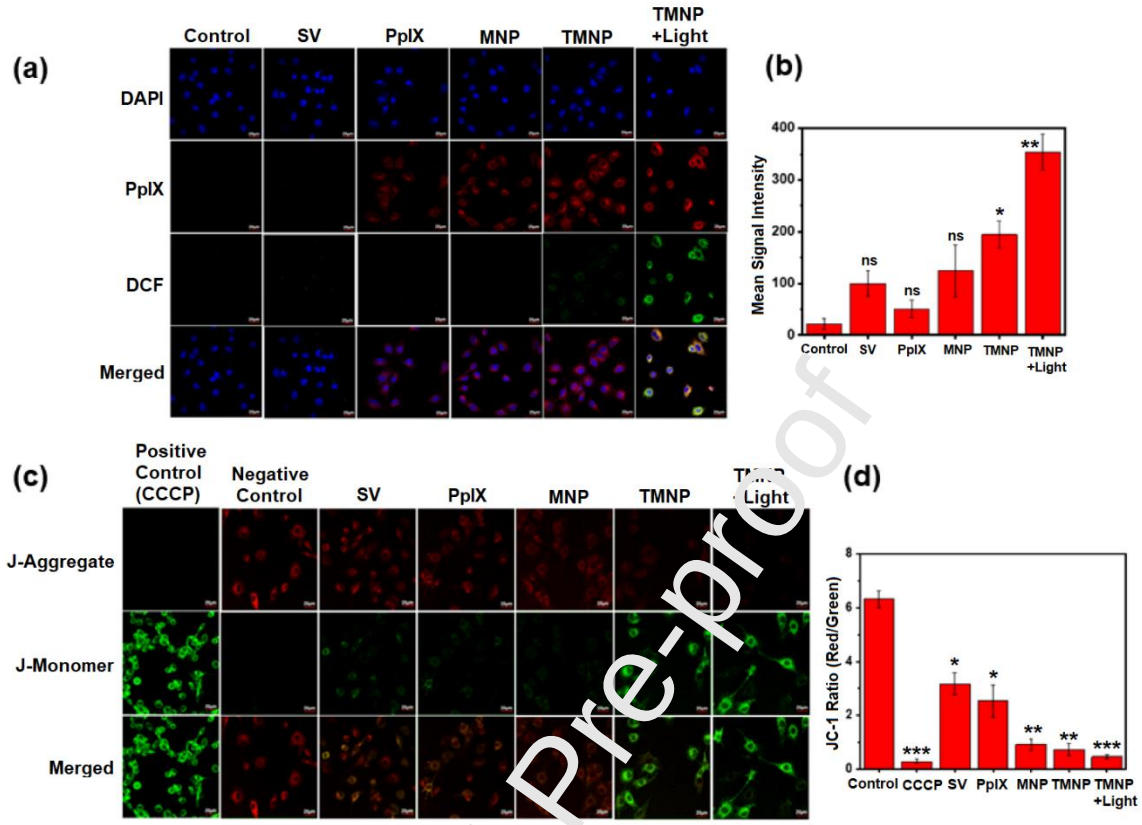

further investigated by CLSM observation. The ROS generation of TMNP with and without irradiation was monitored with an intracellular ROS-detecting probe, namely, 2',7'–dichlorofluorescein diacetate (DCFH-DA) which produces a bright fluorescence at 535 nm after reacting with the reactive oxygen species [62]. As shown in Figure 5a, the other treatment groups except TMNP caused almost no green fluorescence in C6 cells. The slight fluorescence caused by TMNP is justified by the enhanced cellular uptake. However, the cells irradiated after treatment with MNP showed higher fluorescence than cells treated with TMNP alone (Figure S4a). Furthermore, on irradiation of TMNPs, the fluorescence intensity was significantly enhanced due the activation of the released PpIX. ROS generation was quantified using CellRox green reagent and its fluorescence intensity at absorption/emission at 485/520 nm was measured using a microplate reader (Figure 5b). Compare to all treated groups, TMNP + Light irradiated group displayed relatively high fluorescence signal indicating that TMNP + Light is the promising therapeutic nanoprobe for the $^1O_2$ generation.

Figure 5. ROS generation assay: a) Cells were treated with different therapeutic agents and then exposed to a 635-nm laser (130 mW/cm^2 for 5 minutes). ROS generated in C6 cells was measured using DCFH-DA. CSLM

images showing green fluorescence indicate positive staining for ROS. b) Quantitative analysis of ROS generation in cells treated with different agents and then exposed to a 635-nm laser (130mW/cm^2 for 5 minutes) detected using CellRox Green Reagent, JC 1 assay: c) CLSM images representing changes in mitochondria membrane potential when treated with different agents and then exposed to a 635-nm laser (130 mW/cm^2 for 5 minutes). d) Red-to-Green channel ratio of different agents determines the rate of membrane potential decay. *P < 0.05, **P < 0.01 and ***P < 0.001.

3.8 Mitochondrial membrane potential

It has been widely reported that singlet oxygen is highly reactive and causes mitochondrial damage. Thus, we hypothesized that the combination of increased singlet oxygen production by irradiated PpIX and caspase-3 activating SV would cause an enhanced mitochondrial damage. To test this hypothesis, we measured the changes in the mitochondrial membrane potential ($\Delta\psi m$) both quantitatively and qualitatively (Figure 5c and 5d) using the JC-1 assay [63, 64]. $\Delta\psi m$ determines the accumulation of the JC-1, a cationic dye, within the electronegative interior of the mitochondria. At high $\Delta\psi m$, there is an increased concentration of JC-1 in the mitochondria which is indicated by the red fluorescence of the JC-1 aggregates. However, lower $\Delta\psi m$ results in the formation of monomers in the cytosol which emit green fluorescence. The ratio of positive control (CCCP) and negative control was used as a surrogate for analysing the $\Delta\psi m$. As expected, the ratio of the red complex to green monomer decreased for different samples from left to right. After 12 hours of incubation, the cells treated with Free SV, Free PpIX and control group presented a dual staining of green and red fluorescence in the cancer cell cytoplasm. However, for cells treated with MNP and TMNP, the red fluorescence signal gradually becomes weaker while the green fluorescence signal appears, indicating the mitochondrial damage irradiated TMNP which previously showed the highest cellular uptake and greatest ROS production, also exhibited the largest $\Delta\psi m$ in C6 cells, which was significantly greater than the rest of the treatment groups.

3.9 Apoptosis cell study

SV causes cytotoxicity by inducting apoptosis whereas both apoptosis and necrosis are involved in PDT mediated cytotoxicity. By integrating PDT and chemotherapy modalities into a single carrier, TMNP can produce an enhanced apoptosis and necrosis when subjected to light of appropriate wavelength. Due to negligible efflux, SV causes apoptosis by inducing cytochrome C release and subsequent caspase-3 activation and suppresses Akt phosphorylation [22, 65, 66], whereas a high concentration of PpIX accumulates in the cells

to effectively generate ROS upon irradiation thereby causing cell death via both apoptosis and necrosis. It is known that the translocation of phosphatidylserine to the outer layer of the cell membrane marks induction of apoptosis in cancer cells. Hence, we used flow cytometry to quantify the precise extent of apoptosis vs necrosis induced by irradiated TMNP in C6 cells using a dual fluorescence probe Annexin V-FITC (Figure 6a and 6b). The total apoptosis ratio of free SV, MNP and TMNP treated C6 cells was 19.77%, 38.31% and 39.38% respectively. Meanwhile, as expected PpIX without irradiation caused considerably lower apoptosis (9.48%) in the C6 cells. TMNP treated cells subjected to light demonstrated significantly higher apoptosis (49.50%) and necrosis (37.61%) thereby validating our hypothesis that synergistic apoptosis and necrosis plays a major role in the cytotoxicity induced by irradiated TMNP.

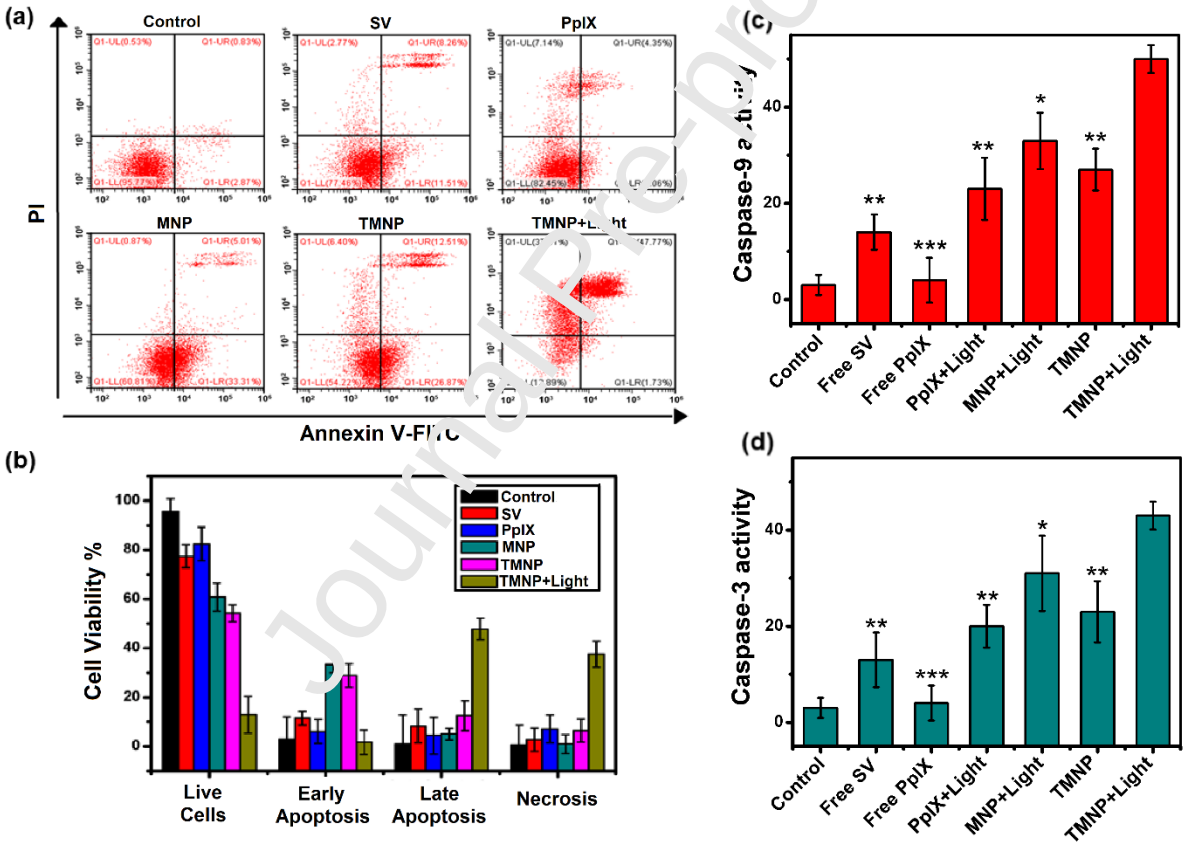

Figure 6. a) Annexin V/PI analysis of C6 cells incubated with DMEM (control), free SV, free PpIX, MNP, TMNP with/without irradiation (635nm laser at 130mW/cm^2 for 5 minutes). The quadrants from lower left to upper left (counter clockwise) represent healthy, early apoptotic, late apoptotic, and necrotic cells, respectively. (b) The percentage of cells in each quadrant was shown on the graphs. c) Caspase-9 activity and d) Caspase-3 activity after treatment with Free SV, Free PpIX, PpIX+Light, MNP+Light, TMNP and TMNP+Light. All the data values are presented as mean ± SD (n = 3). *P < 0.05, **P < 0.01 and ***P < 0.001.

3.10 Caspase 9 and Caspase 3 Activity Assays

The caspase 9 activation dictates the mitochondria-dependent signaling pathway which plays a major role to mediate apoptosis. The activation of caspase-9 and caspase-3 were studied using a colorimetric assay which involves peptide substrates that release the solvatochromic dye p-nitroaniline (pNA)) upon cleavage by a caspase. As shown in Figure 6c and 6d, after 18 h incubation with SV, caspase activity was slightly increased than that of control and PpIX [67, 68]. Compared to drugs without nano-formulation, MNP+Light possess better ability to activate caspase-9 and caspase-3 pathway. However, PpIX+light irradiated and TMNP has similar effects. Whereas, when the cells treated with TMNP+Light, significantly greater caspase release was observed in-comparison to other drug treatment used in the study. This might be obviously due to higher accumulation of TMNP inside the tumour cells facilitated by the surface target ligand-receptor specificity.

3.11 Anti-Angiogenesis Effect of TMNP

It has been demonstrated that tumour cure rates are strongly dependent on vessel damage in and around the treated tumour [48]. Hence, we evaluated the anti-angiogenic potential of TMNP on HUVEC cell line. A comparison between the samples containing only endothelial cells and the treated endothelial cells led us to attribute the anti-angiogenic effects to the functionality of TMNP. It is clearly seen that the control group show neovascular sprouting after 6 hours of incubation (Figure 7a). This is due to the residual growth factors contained in the matrix gel. While PpIX did not inhibit capillary formation, SV and MNP reduced the tube formation and TMNPs produced a greater inhibitory effect on angiogenesis. Furthermore, when subjected to irradiation, TMNPs severely reduced the ability of HUVECs to form capillaries. Further, these general observations was quantified by statistical image analysis using mathematical algorithm AngioQuant (v1.33) [69]. Computer-assisted analysis enables identification of the main vascular network by converting microscopy images to a skeleton. From each image, two parameters were extracted: the mean vessel length and the number of junctions in the skeleton network (Figure 7b and 7c). Both the parameters are drastically compromised when the endothelial cells are treated with irradiated TMNP. This suggests that TMNP has immense potential in tumour reduction as cancerous environments actively accelerate vascularization to obtain adequate nutrients and oxygen for growth and metastasis.

3.12 Cell cycle Arrest

To examine the effect of TMNP on cell cycle distribution, we subjected C6 glioma cells to flow cytometric analysis of total DNA (Figure 7d and 7e). Irradiated TMNP caused a

significant decrease of cells in S phase concomitant with an increase in G_0/G_1 phase compared to control free growing cells. In accordance with previous studies, cells treated with free SV showed a minor increase in their number in G_0/G_1 phase and decrease in the S phase[70, 71]. The increase in the cells in the G_2/M phase caused by inactive PpIX agrees with our previous cytotoxicity data (Figure 2c). There was a considerable increase in the number of cells in the G_0/G_1 stage when treated with TMNP compared to MNP. Interestingly, there was only a slight increase in the number of cells in the G_0/G_1 after PDT, suggesting that PpIX does not contribute much to this mechanism of induced cytotoxicity.

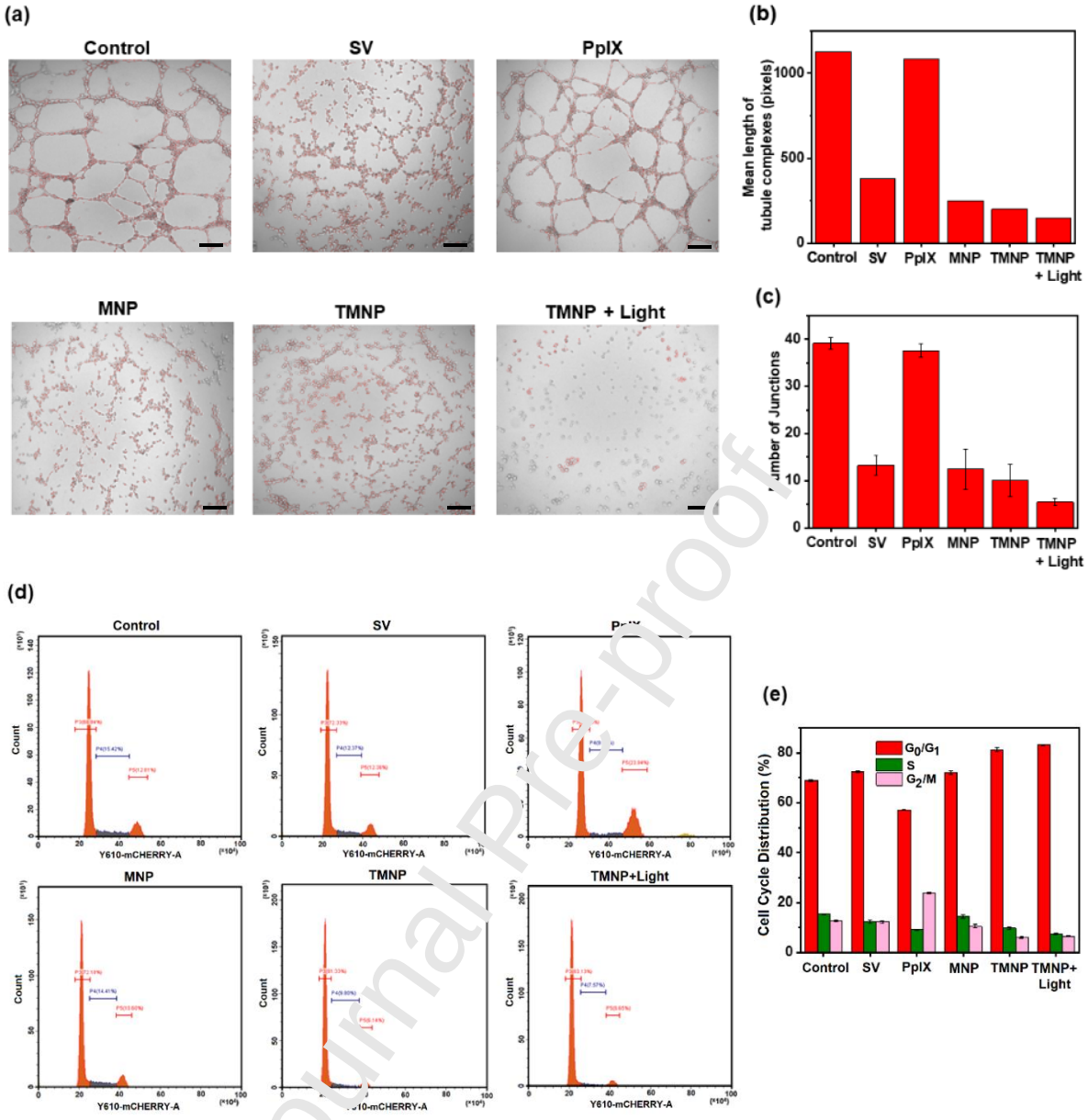

Figure 7. Angiogenesis assay on HUVEC cells: a) Phase contrast images show endothelial cells grown on matrigel after treatment with different agents. Results from computer assisted quantitative analysis of angiogenesis showing b) mean length of tubule complexes and c) number of junctions. Effect of different agents on cell cycle progression: d) The cell cycle distribution was determined by a flow cytometric analysis of the DNA content after staining with propidium iodide. e) Data expressed as mean ± SD from three independent experiments. *P < 0.05, **P < 0.01, ***P < 0.001 and ns – Not Significant.

3.13 Growth Inhibitory Effect on C6 Spheroids

MCs are of clinical relevance in the study of DDSs, as they mimic the cellular microenvironments such as hypoxia, cell-cell interactions occurring in-vivo, presence of extracellular matrix (ECM) and diffusional constraints. All of these factors can reduce the

efficacy of the DDS either by inducing drug resistance via the local microenvironment or by mass transport limitations. Figure 8a shows the representative optical images of MCs treated with free SV, free PpIX, MNP, TMNP and TMNP with light. While the diameter of the MCs treated with fresh medium continued to increase over time due to secretion of ECM and interaction between the cells, the diameter of the MCs treated with free PpIX and free SV remained almost constant. MNP showed a slight decrease in the diameter compared to TMNP, which exerted a greater inhibitory effect on the MCs. However, once the MCs could restore their proliferation conditions after ~5 days, the diameter of the MCs exposed to these treatment groups increased. Furthermore, metastatic spheroids resulting from collective detachment from the primary tumours were observed for these treatment groups at day 7 [72]. In contrast, the decrease in diameter of TMNP treated MCs irradiated with a 130 mW/cm^2 630-nm laser at day 2, was monotonical during the whole test. Figure 8b depicts the change in average volume of MCs in 6 groups as a function of time. The control groups showed a significant increase in volume over the 7 days. This can be attributed to the proliferation of the outer layer of the MCs. After day 5, the volume of MCs reaches a plateau. No significant difference in volume was observed following exposure to free SV, free PpIX and MNP. The volume of MCs treated with TMNP begins to increase after day 5, whereas the volume of MCs exposed to TMNP + Light significantly reduces even after day 5. In line with our cytotoxicity data on 2D monolayer cultures (Figure 2), these results suggest that targeted carriers are not very effective if they rely on monotherapy alone, and should be able to leverage on combination therapies such as chemophototherapy.

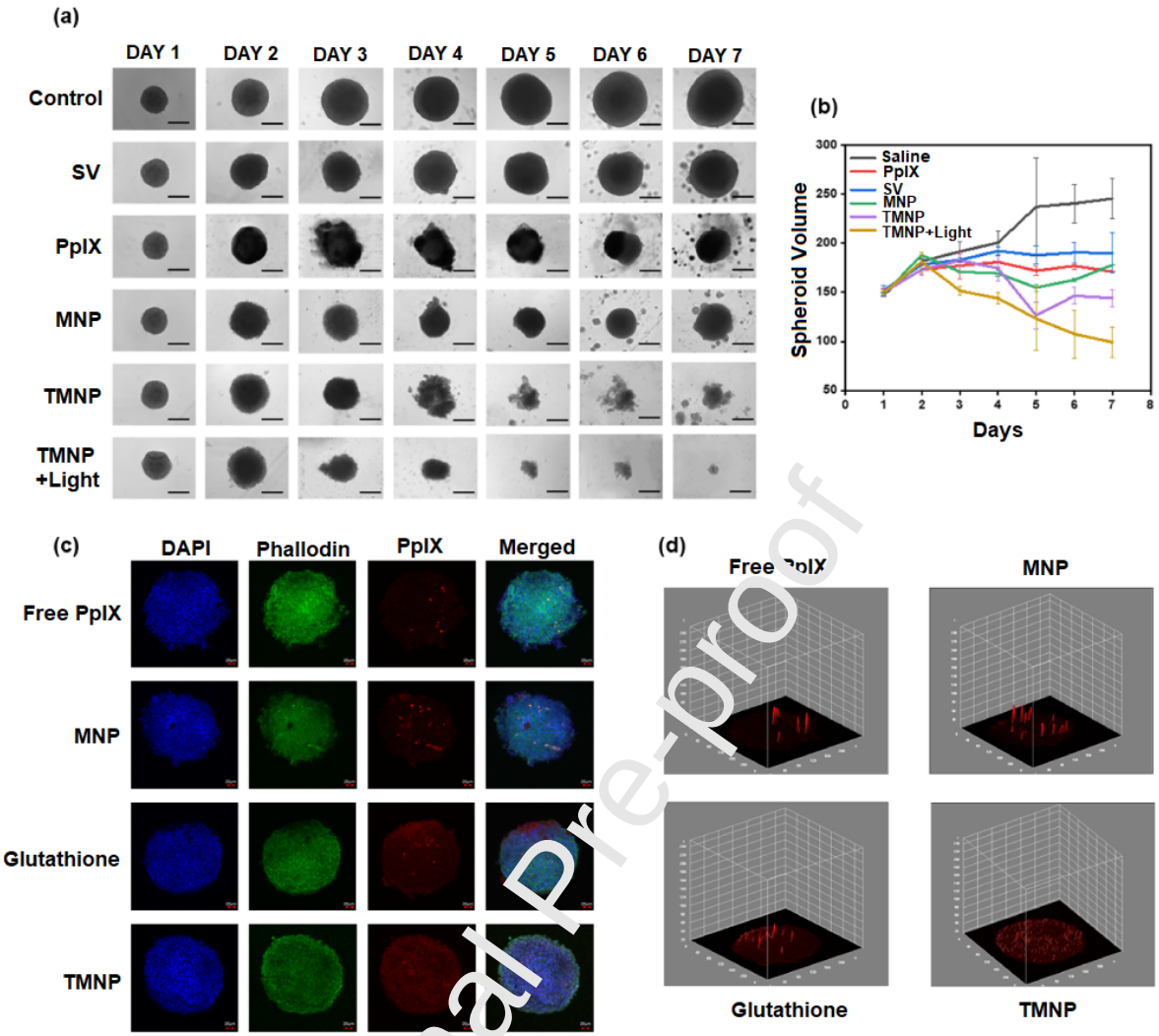

Figure 8. Growth Inhibition assay in C6 MCs: a) Sequential Bright-field images of the same C6 spheroids treated with free SV, free PpIX, MNP, TMNP, TMNP+light (Scale bar = 275µm), b) Volume changes of MCs over 7 days. Data represents average ± standard deviation of three (n=3) independent measurements. Penetration and Distribution in C6 spheroids: c) CLSM images of C6 MCs treated with Free PpIX, PpIX+Micelles, PpIX+T-Micelles and C6 MCs pre-incubated with Glutathione (1mg/ml) before treatment with PpIX+T-Micelles for 6 hours. Scale bar, 20 µm, d) Surface plots of images in (a), produced in Image J.

3.14 Penetration and Distribution in C6 Spheroids

Many researchers leverage on the EPR effect when discussing translation of in-vitro results to in-vivo efficacy for DDSs. However, the conventional understanding of EPR is greatly simplified in comparison to the in-vivo tumour microenvironment. Barriers such as limited access to tumour cells and penetration need to be overcome to achieve in-vivo success [73, 74]. C6 tumour spheroids of ~400-450µm which consists of an inner quiescent layer and an outer proliferating cell layer, mimics the 3D in-vivo environment due to limited oxygen and

nutrient transport [75, 76]. The MCs were exposed to free PpIX, MNP and TMNP and examined over time via CLSM to evaluate the ability of the proposed DDS to infiltrate into the 3D structure (Figure 8c). The penetration and distribution of free PpIX in the MCs were restricted to the boundary layers after 6 hours (Figure 8d). The fluorescence intensity of MNP show deeper penetration into MCs compared to the free payload. Compared to free PpIX and MNP, TMNPs show a strong fluorescence signal extending from the periphery to the center of the MCs within 6 h. This suggests that Glutathione conjugation can facilitate deeper penetration of the micelles into the solid tumours. To confirm our findings, we pre-incubated the MCs overnight at 1mg/ml of Glutathione and then treated with TMNP for 6 h. The images suggest that majority of the fluorescence signal is localized in the around the boundary of the spheroids compared to those without pre-treatment.

3.15 Effect on Spheroid Morphology

The control group of C6 spheroids showed evidence of normal morphological features of nuclear chromatin, intact nuclear membrane, mitochondria display membrane-enclosed filamentous cristae, secretory material rich cytoplasm, intact cytoplasmic membrane, and numerous microvilli communicating with other cells (Figure 9a, b and c). Furthermore, the TEM images clearly show the presence of extracellular matrix in the intracellular space and the surface of the cells, suggesting stabilized cell-ECM and cell-cell interactions [77]. The C6 spheroids treated with TMNP show a smooth cell surface/short microvillus but compact nuclear membrane. Additionally, distinct apoptosis features were observed such as fragmented nuclear content, loss of membrane-enclosed filamentous cristae in the mitochondria, and a greater number of vacuoles in the cytoplasm (Figure 9d, e and f). This result further confirms that the mitochondrial damage could be associated with abundant ROS production through PDT therapy.

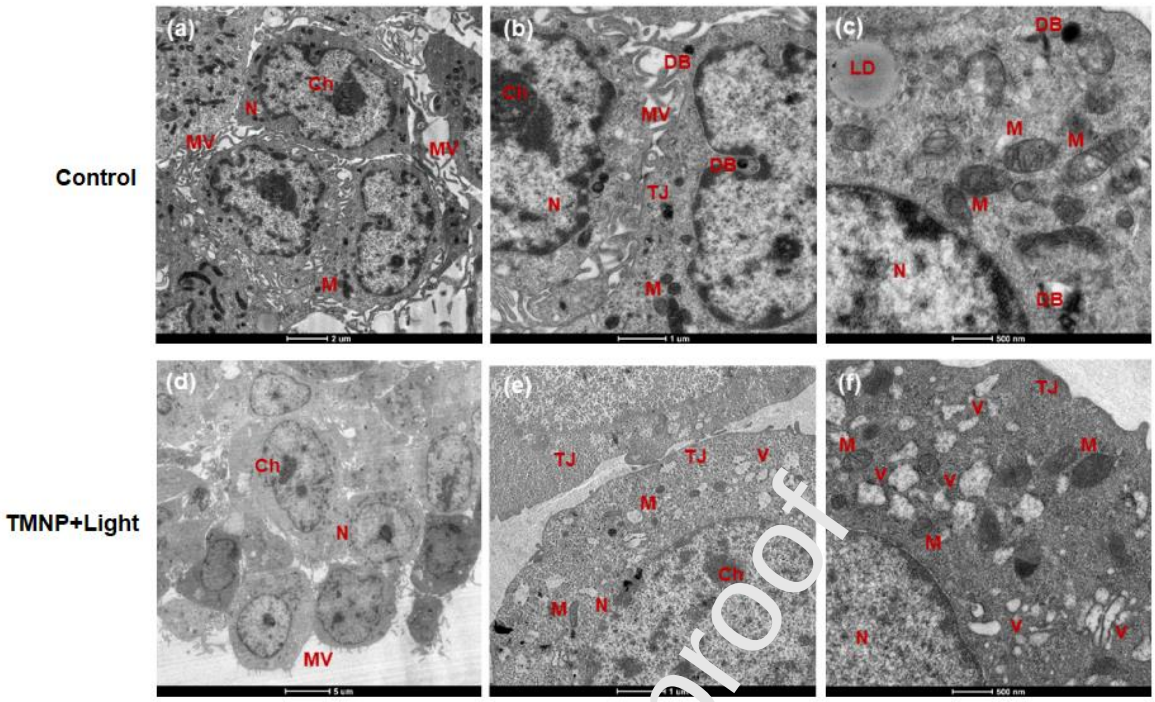

Figure 9. TEM image of C6 tumour spheroids after 36 h culturing (a, b and c) Control group (d, e and f) Spheroids treated with TMNP at a concentration of 6.293 µg/mL for 12 h. Ch: chromatin; DB: Dense body; LD: Lipid droplet; M: Mitochondria; MV: Microvillus; N: Nucleus; TJ: Tight junction; V: vacuole.

3.16 Delivery and Accumulation of TMNP within the tumour

The mathematical model given in Section 2.21 is applied to predict the delivery outcomes using TMNP and MNP, respectively. Model parameters describing the transport properties of the two nanoprobes are summarised in Table 1. For comparison, their intravascular concentrations are assumed to be identical.

The concentration profiles of TMNP and MNP from the blood vessel wall into deep tumour are compared in different tissue compartments in Figure 10a. TMNP is found with the higher C_{ECS} near the blood vessel wall. This is owing to the enhanced BBB penetration induced by Glutathione. As a consequence, more TMNPs could enter the tumour ECS and thereby improve the drug accumulation both on CM and in ICS, as shown in Figure 10a(ii) and (iii).

Figure 10b(i) compares the spatial averaged concentrations of TMNP and MNP. Results indicate that the drug accumulation using TMNP is more effective in all the three tissue compartments. Similarly, drugs are able to penetrate into deeper tumour regions when loaded into TMNP, as implied in Figure 10b(ii).

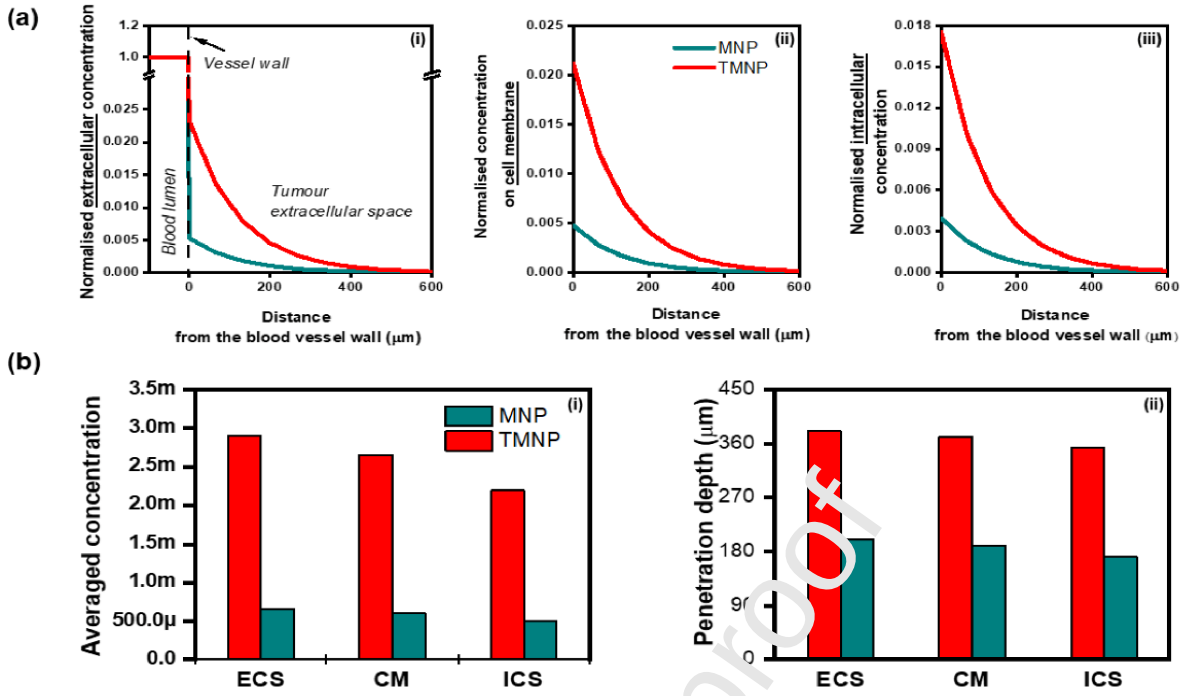

Figure 10. a) Comparison of TMNP and MNP concentration in each tissue compartment as a function of distance from blood vessel wall. Concentration i) in ECS, ii) on CM and iii) in ICS of tumour tissue, normalised by C_{IVS}. b) Comparison of TMNP and MNP delivery outcome in each tissue compartiment. i) Spatial averaged concentration, which is normalised by C_{IVS}. ii) Penetration depth which is counted when the local concentration is greater than 0.1% of C_{IVS}.

4. Conclusions

Chemotherapeutic agents such as simvastatin and photosensitizers such as protoporphyrin IX suffer from poor penetration into solid tumours, resulting in ineffective treatments due to exposure to sublethal drug concentrations and subsequent development of drug resistance [78]. DDSs developed to combat this issue has several advantages such as reduced systemic exposure and improved pharmacokinetics but still suffers from poor in-vivo efficacy. 3D multicellular spheroids which closely represent the in-vivo environment, can be used as an intermediate tool to evaluate the therapeutic effect of the DDSs before proceeding to animal models. In this paper, we have fabricated a PE-PEG based nanotherapeutic probe that integrates two treatment modalities, chemotherapy and PDT, into a single DDS for a synergistic anticancer activity in 3D multicellular spheroids. We extensively characterized the colloidal stability, drug loading and the release behaviour of SV and PpIX over a period of a few days. TMNP has several distinctive capabilities: (i) Possesses synthetic convenience and good biocompatibility, (ii) Exceptionally high loading of SV and PpIX, which is released in the acidic tumour microenvironment, (iii) Can potentially be used for image guided therapy to identify optimum location to release the therapeutic payload, (iv) Possesses multiple killing mechanisms – synergistic apoptosis, necrosis, anti-angiogenesis and cell

cycle arrest, (v) Exhibited negligible dark toxicity thereby providing a truly controllable treatment option. (vi) Enhanced penetration into solid tumours, validated by both experimental and modelling results. Overall, this integrated treatment platform reduces side effects, overcomes the low efficiency of PDT in hypoxia cells, and retards multidrug resistance of chemotherapeutics. The promising insights provided by this targeted and image-guided combination therapy warrants further evaluation of its therapeutic efficacy in animal models. However, the clinical translation of PDT is hindered due to the limited penetration range of visible light into tissues and there is a need to develop strategies such as the use of external optical fibers to ensure precise and adequate dispersion of light within the brain tumours [79].

Acknowledgements

Chi-Hwa Wang is supported by National Additive Manufacturing Innovation Cluster @ National University of Singapore. Nitish V. Thakor is supported by Singapore National Research Foundation, Award No.: NRF-CRP15-2015-04. Vishnu Sunil greatly appreciates the National University of Singapore Research Scholarship for the funding of his Ph.D. studies in the National University of Singapore.

References

1. Hu, D., et al., *Oxygen-generating hybrid polymeric nanoparticles with encapsulated doxorubicin and chlorin e6 for trimodal imaging-guided combined chemo-photodynamic therapy.* Theranostics, 2018. **8**(6): p. 1558.
2. Ong, B.Y., et al., *Paclitaxel delivery from PLGA foams for controlled release in post-surgical chemotherapy against glioblastoma multiforme.* Biomaterials, 2009. **30**(18): p. 3189-3196.
3. Davoodi, P., et al., *Drug delivery systems for programmed and on-demand release.* Advanced drug delivery reviews, 2018. **132**: p. 104-138.
4. Wang, J., et al., *Activatable ferritin nanocomplex for real-time monitoring of caspase-3 activation during photodynamic therapy.* ACS applied materials & interfaces, 2015. **7**(41): p. 23248-23256.
5. Zhang, L., et al., *A porphyrin photosensitized metal–organic framework for cancer cell apoptosis and caspase responsive theranostics.* Chemical Communications, 2015. **51**(54): p. 10831-10834.
6. Chatzinikolaidou, M., *Cell spheroids: the new frontiers in in vitro models for cancer drug validation.* Drug discovery today, 2016. **21**(9): p. 1553-1560.
7. Zips, D., H.D. Thames, and M. BAUMANN, *New anticancer agents: in vitro and in vivo evaluation.* in vivo, 2005. **19**(1): p. 1-7.
8. Netti, P.A., et al., *Role of extracellular matrix assembly in interstitial transport in solid tumors.* Cancer research, 2000. **60**(9): p. 2497-2503.
9. Goodman, T.T., C.P. Ng, and S.H. Pun, *3-D tissue culture systems for the evaluation and optimization of nanoparticle-based drug carriers.* Bioconjugate chemistry, 2008. **19**(10): p. 1951-1959.
10. Pluen, A., et al., *Role of tumor–host interactions in interstitial diffusion of macromolecules: cranial vs. subcutaneous tumors.* Proceedings of the National Academy of Sciences, 2001. **98**(8): p. 4628-4633.
11. Goodman, T.T., P.L. Olive, and S.H. Pun, *Increased nanoparticle penetration in collagenase-treated multicellular spheroids.* International journal of nanomedicine, 2007. **2**(2): p. 265.
12. Breslin, S. and L. O'Driscoll, *Three-dimensional cell culture: the missing link in drug discovery.* Drug discovery today, 2013. **18**(5-6): p. 240-249.
13. Doke, S.K. and S.C. Dhawale, *Alternatives to animal testing: A review.* Saudi Pharmaceutical Journal, 2015. **23**(3): p. 223-229.
14. Menshykau, D., *Emerging technologies for prediction of drug candidate efficacy in the preclinical pipeline.* Drug discovery today, 2017. **22**(11): p. 1598-1603.
15. Chen, Q., et al., *Albumin-NIR dye self-assembled nanoparticles for photoacoustic pH imaging and pH-responsive photothermal therapy effective for large tumors.* Biomaterials, 2016. **98**: p. 23-30.
16. Zhou, Q., et al., *Co-delivery nanoparticle to overcome metastasis promoted by insufficient chemotherapy.* Journal of controlled release, 2018. **275**: p. 67-77.
17. Minchinton, A.I. and I.F. Tannock, *Drug penetration in solid tumours.* Nature Reviews Cancer, 2006. **6**(8): p. 583.
18. Zhao, C., et al., *"Sheddable" PEG-lipid to balance the contradiction of PEGylation between long circulation and poor uptake.* Nanoscale, 2016. **8**(20): p. 10832-10842.
19. Zhou, X.X., et al., *pH-responsive polymeric micelles self-assembled from amphiphilic copolymer modified with lipid used as doxorubicin delivery carriers.* Royal Society open science, 2018. **5**(3): p. 171654.
20. Fortuny, J., et al., *Statin use and risk of lymphoid neoplasms: results from the European Case-Control Study EPILYMPH.* Cancer Epidemiology and Prevention Biomarkers, 2006. **15**(5): p. 921-925.

21. Xu, Q., et al., *Application of statins in management of glioma: Recent advances.* Tropical Journal of Pharmaceutical Research, 2018. **17**(7): p. 1445-1451.
22. Koyuturk, M., M. Ersoz, and N. Altiok, *Simvastatin induces proliferation inhibition and apoptosis in C6 glioma cells via c-jun N-terminal kinase.* Neuroscience letters, 2004. **370**(2-3): p. 212-217.
23. Seliger, C., et al., *Use of statins or NSAIDs and survival of patients with high-grade glioma.* PLOS ONE, 2018. **13**(12): p. e0207858.
24. Li, G., et al., *Simvastatin inhibits tumor angiogenesis in HER2-overexpressing human colorectal cancer.* Biomedicine & Pharmacotherapy, 2017. **85**: p. 418-424.
25. Hata, Y., et al., *Antiangiogenic mechanisms of simvastatin in retinal endothelial cells.* Graefe's Archive for Clinical and Experimental Ophthalmology, 2010. **248**(5): p. 667-673.
26. Shen, W., et al., *The effects of simvastatin on angiogenesis: studied by an original model of atherosclerosis and acute myocardial infarction in rabbit.* Molecular Biology Reports, 2011. **38**(6): p. 3821-3828.
27. Skaletz-Rorowski, A., et al. *The pro-and antiangiogenic effects of statins*. in *Seminars in vascular medicine*. 2004. Copyright© 2004 by Thieme Medical Publishers, Inc., 333 Seventh Avenue, New ….
28. Verma, S., et al., *Strategies for enhanced photodynamic therapy effects.* Photochemistry and photobiology, 2007. **83**(5): p. 996-1005.
29. Yan, L., et al., *Protoporphyrin IX (PpIX)-Coated Superparamagnetic Iron Oxide Nanoparticle (SPION) Nanoclusters for Magnetic Resonance Imaging and Photodynamic Therapy.* Advanced functional materials, 2018. **28**(16): p. 1707030.
30. Northrop, B.H., S.H. Frayne, and U. Choudhary, *Thiol–maleimide "click" chemistry: evaluating the influence of solvent, initiator, and thiol on the reaction mechanism, kinetics, and selectivity.* Polymer Chemistry, 2015. **6**(18): p. 3415-3430.
31. Ashok, B., et al., *In vitro characterization of PEGylated phospholipid micelles for improved drug solubilization: effects of PEG chain length and PC incorporation.* Journal of pharmaceutical sciences, 2004. **93**(10): p. 2476-2487.
32. Su, J., et al., *Catechol Polymers for pH-Responsive, Targeted Drug Delivery to Cancer Cells.* Journal of the American Chemical Society, 2011. **133**(31): p. 11850-11853.
33. Tian, T., et al., *Targeted Imaging of Brain Tumors with a Framework Nucleic Acid Probe.* ACS Applied Materials & Interfaces, 2018. **10**(4): p. 3414-3420.
34. Mikhail, A.S., S. Eetezadi, and C. Allen, *Multicellular tumor spheroids for evaluation of cytotoxicity and tumor growth inhibitory effects of nanomedicines in vitro: a comparison of docetaxel-loaded block copolymer micelles and Taxotere®.* PloS one, 2013. **8**(4).
35. Zhan, W. and C.-H. Wang, *Convection enhanced delivery of chemotherapeutic drugs into brain tumour.* Journal of Controlled Release, 2018. **271**: p. 74-87.
36. Wu, N.Z., et al., *Increased microvascular permeability contributes to preferential accumulation of Stealth liposomes in tumor tissue.* Cancer Res, 1993. **53**(16): p. 3765-70.
37. Yuan, F., et al., *Microvascular permeability and interstitial penetration of sterically stabilized (stealth) liposomes in a human tumor xenograft.* Cancer Res, 1994. **54**(13): p. 3352-6.
38. Jain, R.K., *Transport of molecules in the tumor interstitium: a review.* Cancer research, 1987. **47**(12): p. 3039-3051.
39. Jin, H., et al., *Size-dependent cellular uptake and expulsion of single-walled carbon nanotubes: single particle tracking and a generic uptake model for nanoparticles.* ACS nano, 2009. **3**(1): p. 149-158.
40. Lauffenburger, D.A. and J.J. Linderman, *Receptors: models for binding, trafficking, and signaling*. 1996: Oxford University Press on Demand.
41. Afadzi, M., et al. *Ultrasound stimulated release of liposomal calcein*. in *Ultrasonics Symposium (IUS), 2010 IEEE*. 2010. IEEE.

42. Corsi, L., A. Mescola, and A. Alessandrini, *Glutamate receptors and glioblastoma multiforme: an old "route" for new perspectives.* International journal of molecular sciences, 2019. **20**(7): p. 1796.
43. Van Vuurden, D.G., et al., *Attenuated AMPA receptor expression allows glioblastoma cell survival in glutamate-rich environment.* PLoS One, 2009. **4**(6).
44. Liu, X., et al., *Effects of blockade of ionotropic glutamate receptors on blood–brain barrier disruption in focal cerebral ischemia.* Neurological sciences, 2010. **31**(6): p. 699-703.
45. Macrez, R., et al., *Neuroendothelial NMDA receptors as therapeutic targets in experimental autoimmune encephalomyelitis.* Brain, 2016. **139**(9): p. 2406-2419.
46. Englert, C., et al., *Crossing the blood-brain barrier: Glutathione-conjugated poly (ethylene imine) for gene delivery.* Journal of Controlled Release, 2016. **241**: p. 1-14.
47. Fatima, S., et al., *Identification and evaluation of glutathione conjugate gamma-l-glutamyl-l-cysteine for improved drug delivery to the brain.* Journal of Biomolecular Structure and Dynamics, 2019: p. 1-11.
48. Ahmad, Z., et al., *Polymeric micelles as drug delivery vehicles.* RSC Advances, 2014. **4**(33): p. 17028-17038.
49. Cui, P.-F., et al., *A new strategy for hydrophobic drug delivery using a hydrophilic polymer equipped with stacking units.* Chemical Communications, 2018. **54**(59): p. 8218-8221.
50. Wei, X., et al., *Codelivery of a π–π stacked dual anticancer drug combination with nanocarriers for overcoming multidrug resistance and tumor metastasis.* Advanced Functional Materials, 2016. **26**(45): p. 8266-8280.
51. Poinard, B., et al., *Polydopamine Nanoparticles Enhance Drug Release for Combined Photodynamic and Photothermal Therapy.* ACS Applied Materials & Interfaces, 2018. **10**(25): p. 21125-21136.
52. Vinluan, R.D., et al., *Glutathione-Coated Luminescent Gold Nanoparticles: A Surface Ligand for Minimizing Serum Protein Adsorption.* ACS Applied Materials & Interfaces, 2014. **6**(15): p. 11829-11833.
53. Ding, H., et al., *Nanoscopic micelle delivery improves the photophysical properties and efficacy of photodynamic therapy of protoporphyrin IX.* Journal of Controlled Release, 2011. **151**(3): p. 271-277.
54. Dubois, L.G., et al., *Gliomas and the vascular fragility of the blood brain barrier.* Frontiers in cellular neuroscience, 2014. **8**: p. 418-418.
55. Brown, R.C., A.P. Morris, and R.G. O'Neil, *Tight junction protein expression and barrier properties of immortalized mouse brain microvessel endothelial cells.* Brain Research, 2007. **1130**: p. 17-30.
56. Omidi, Y., et al., *Evaluation of the immortalised mouse brain capillary endothelial cell line, b.End3, as an in vitro blood–brain barrier model for drug uptake and transport studies.* Brain Research, 2003. **990**(1): p. 95-112.
57. Kannan, R., et al., *Evidence for carrier-mediated transport of glutathione across the blood-brain barrier in the rat.* The Journal of clinical investigation, 1990. **85**(6): p. 2009-2013.
58. Rip, J., et al., *Glutathione PEGylated liposomes: pharmacokinetics and delivery of cargo across the blood–brain barrier in rats.* Journal of drug targeting, 2014. **22**(5): p. 460-467.
59. Geldenhuys, W., et al., *Brain-targeted delivery of paclitaxel using glutathione-coated nanoparticles for brain cancers.* Journal of drug targeting, 2011. **19**(9): p. 837-845.
60. Mettlen, M., et al., *Dissecting dynamin's role in clathrin-mediated endocytosis.* Biochem Soc Trans, 2009. **37**(Pt 5): p. 1022-6.
61. Henley, J.R., et al., *Dynamin-mediated internalization of caveolae.* The Journal of cell biology, 1998. **141**(1): p. 85-99.
62. Mozhi, A., et al., *Nrp-1 receptor targeting peptide-functionalized TPGS micellar nanosystems to deliver 10-hydroxycampothecin for enhanced cancer chemotherapy.* International journal of pharmaceutics, 2018. **547**(1-2): p. 582-592.

63. Mozhi, A., et al., *pH-sensitive polymeric micelles for the Co-delivery of proapoptotic peptide and anticancer drug for synergistic cancer therapy.* RSC Advances, 2017. **7**(21): p. 12886-12896.
64. Tuguntaev, R.G., et al., *P-gp inhibition and mitochondrial impairment by dual-functional nanostructure based on vitamin E derivatives to overcome multidrug resistance.* ACS applied materials & interfaces, 2017. **9**(20): p. 16900-16912.
65. Wu, H., et al., *Effect of simvastatin on glioma cell proliferation, migration, and apoptosis.* Neurosurgery, 2009. **65**(6): p. 1087-1097.
66. Koyuturk, M., M. Ersoz, and N. Altiok, *Simvastatin induces apoptosis in human breast cancer cells: p53 and estrogen receptor independent pathway requiring signalling through JNK.* Cancer letters, 2007. **250**(2): p. 220-228.
67. Yanae, M., et al., *Statin-induced apoptosis via the suppression of ERK1/2 and Akt activation by inhibition of the geranylgeranyl-pyrophosphate biosynthesis in glioblastoma.* Journal of Experimental & Clinical Cancer Research, 2011. **30**(1): p. 74.
68. Alizadeh, J., et al., *Mevalonate cascade inhibition by simvastatin induces the intrinsic apoptosis pathway via depletion of isoprenoids in tumor cells.* Scientific reports, 2017. **7**: p. 44841.
69. Niemisto, A., et al., *Robust quantification of in vitro angiogenesis through image analysis.* IEEE transactions on medical imaging, 2005. **24**(4): p. 549-553.
70. Relja, B., et al., *Simvastatin inhibits cell growth and induces apoptosis and G0/G1 cell cycle arrest in hepatic cancer cells.* International journal of molecular medicine, 2010. **26**(5): p. 735-741.
71. Soma, M.R., et al., *PKC activity in rat C6 glioma cells: changes associated with cell cycle and simvastatin treatment.* Biochemical and biophysical research communications, 1994. **200**(2): p. 1143-1149.
72. Al Habyan, S., et al., *Multicellular detachment generates metastatic spheroids during intra-abdominal dissemination in epithelial ovarian cancer.* Oncogene, 2018. **37**(37): p. 5127-5135.
73. Ruoslahti, E., S.N. Bhatia, and M.J. Sailor, *Targeting of drugs and nanoparticles to tumors.* Journal of Cell Biology, 2010. **188**(6): p. 759-768.
74. Lammers, T., et al., *Drug targeting to tumors: principles, pitfalls and (pre-) clinical progress.* Journal of controlled release, 2012. **161**(2): p. 175-187.
75. Mehta, G., et al., *Opportunities and challenges for use of tumor spheroids as models to test drug delivery and efficacy.* Journal of Controlled Release, 2012. **164**(2): p. 192-204.
76. Zelenkov, P., et al., *Acute morphological sequelae of photodynamic therapy with 5-aminolevulinic acid in the C6 spheroid model.* Journal of neuro-oncology, 2007. **82**(1): p. 49.
77. Wang, X., et al., *Doxorubicin delivery to 3D multicellular spheroids and tumors based on boronic acid-rich chitosan nanoparticles.* Biomaterials, 2013. **34**(19): p. 4667-4679.
78. Dhanikula, R.S., et al., *Methotrexate loaded polyether-copolyester dendrimers for the treatment of gliomas: enhanced efficacy and intratumoral transport capability.* Molecular pharmaceutics, 2008. **5**(1): p. 105-116.
79. Chen, M.-H., et al., *Non-invasive Photodynamic Therapy in Brain Cancer by Use of Tb3+-Doped LaF3 Nanoparticles in Combination with Photosensitizer Through X-ray Irradiation: A Proof-of-Concept Study.* Nanoscale Research Letters, 2017. **12**(1): p. 62.

Author Contributions:

Chi-Hwa Wang and Nitish V. Thakor: Conceptualization. Anbu Mozhi, Vishnu Sunil, Wenbo Zhan, and Pramila Baban Ghode designed the experiments. Anbu Mozhi and Vishnu Sunil performed the experiments. Anbu Mozhi, Vishnu Sunil, and Wenbo Zhan analysed the data. Anbu Mozhi and Vishnu Sunil wrote the manuscript. All authors reviewed the revised manuscript.

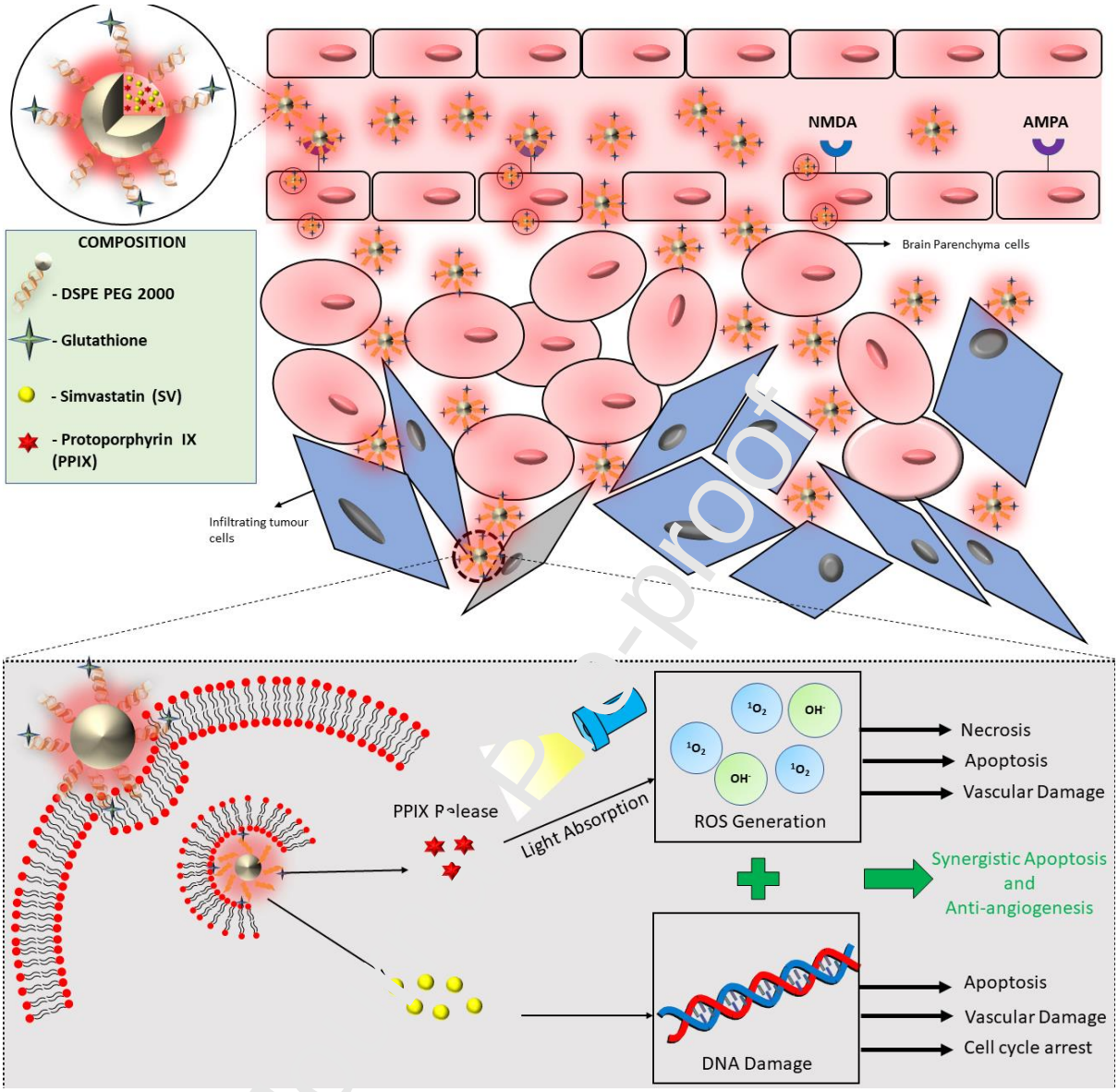

Scheme 1. Proposed cytotoxicity mechanism of TMNP. Schematic showing high concentration of TMNP surrounding the tumour by leveraging on receptor mediated endocytosis and leaky vasculature of the BBB.

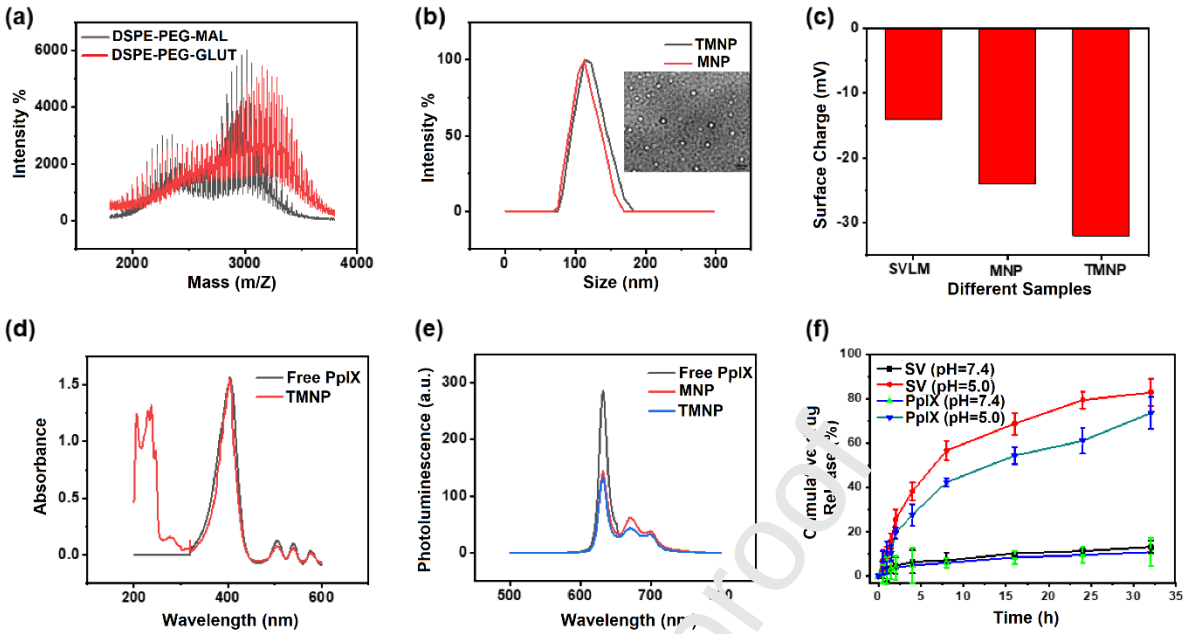

Figure 1. Characterization: a) MALDI-TOF spectra of DSPE-PEG-MAL (black) and DSPE-PEG-GLUT (red). b) Hydrodynamic diameter (DH) histogram distribution profile of TMNP (black) and MNP (red), (inset) TEM image of TMNP, Scale bar 200 nm. c) Zeta potential of SVLM, MNP and TMNP. d) Absorbance spectra of free PpIX (black) and TMNP (red). e) Fluorescence emission spectra after excitation at 405 nm of free PpIX (black) and TMNP (red). f) Release of SV and PpIX from TMNP over time in of different pH solutions. (SVLM = Simvastatin loaded micelles; MNP = SV and PpIX loaded Micellar nanoprobe; TMNP = SV and PpIX loaded Targeted Micellar nanoprobe).

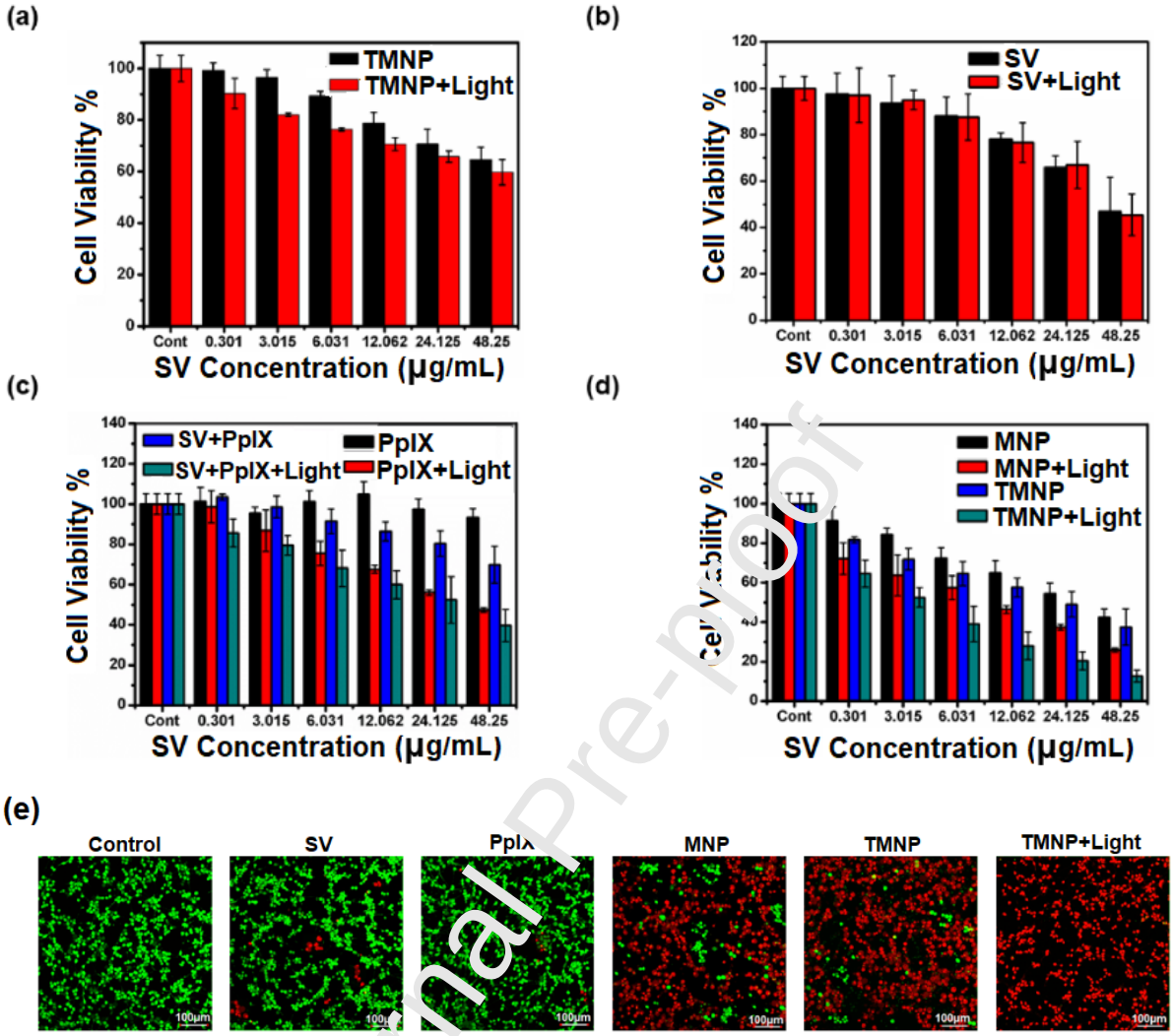

Figure 2. In vitro cancer cell killing efficacy of TMNP. Cell viability after dosing a) 3T3 and b, c, and d) C6 cells with varying concentrations of treatment groups with/without irradiation (635 nm laser at 130 mW/cm2 for 5 minutes) in a medium supplemented with serum for 24 hours. (n = 3), e) CLSM photographs of C6 cells received different treatments. Calcein AM and ethidium homodimer-1 staining was performed for live cells (green) and dead cells (red) respectively. Scale bar, 100 µm.

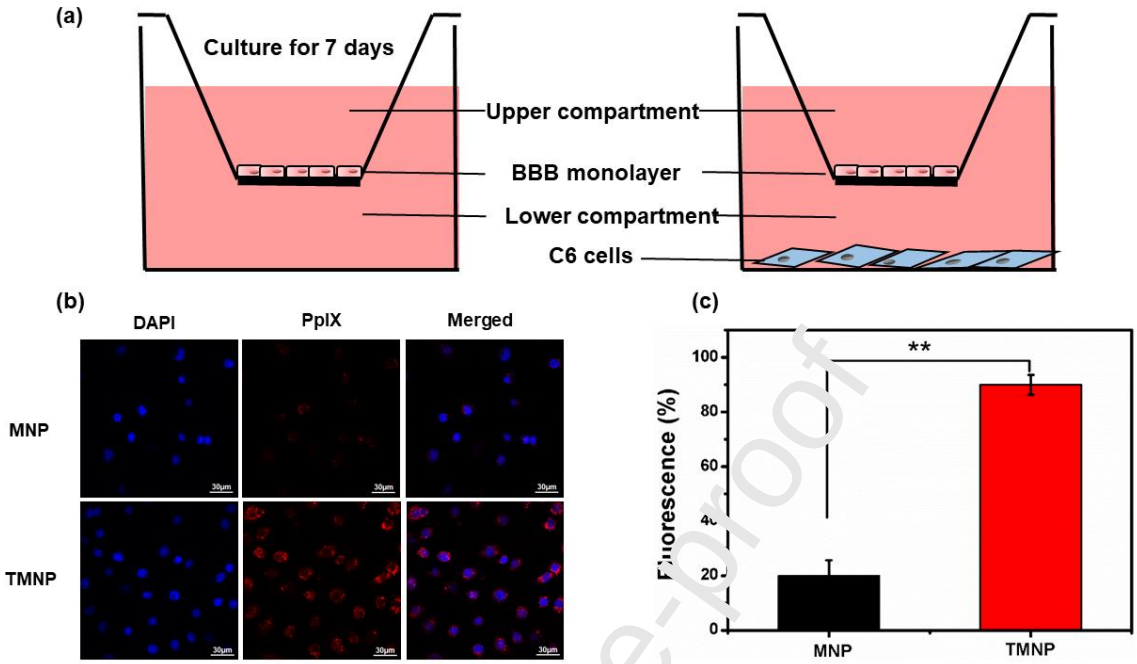

Figure 3. In-vitro BBB penetration study. a) Schematic representation of the in-vitro BBB model. b) CLSM photographs of MNP and TMNP in C6 cells after transporting across the BBB model. c) Fluorescent statistic of C6 cell uptake efficiency of MNP and TMNP after transporting across the BBB model. Scale bar, 20 μm **P < 0.01 and ***P < 0.001

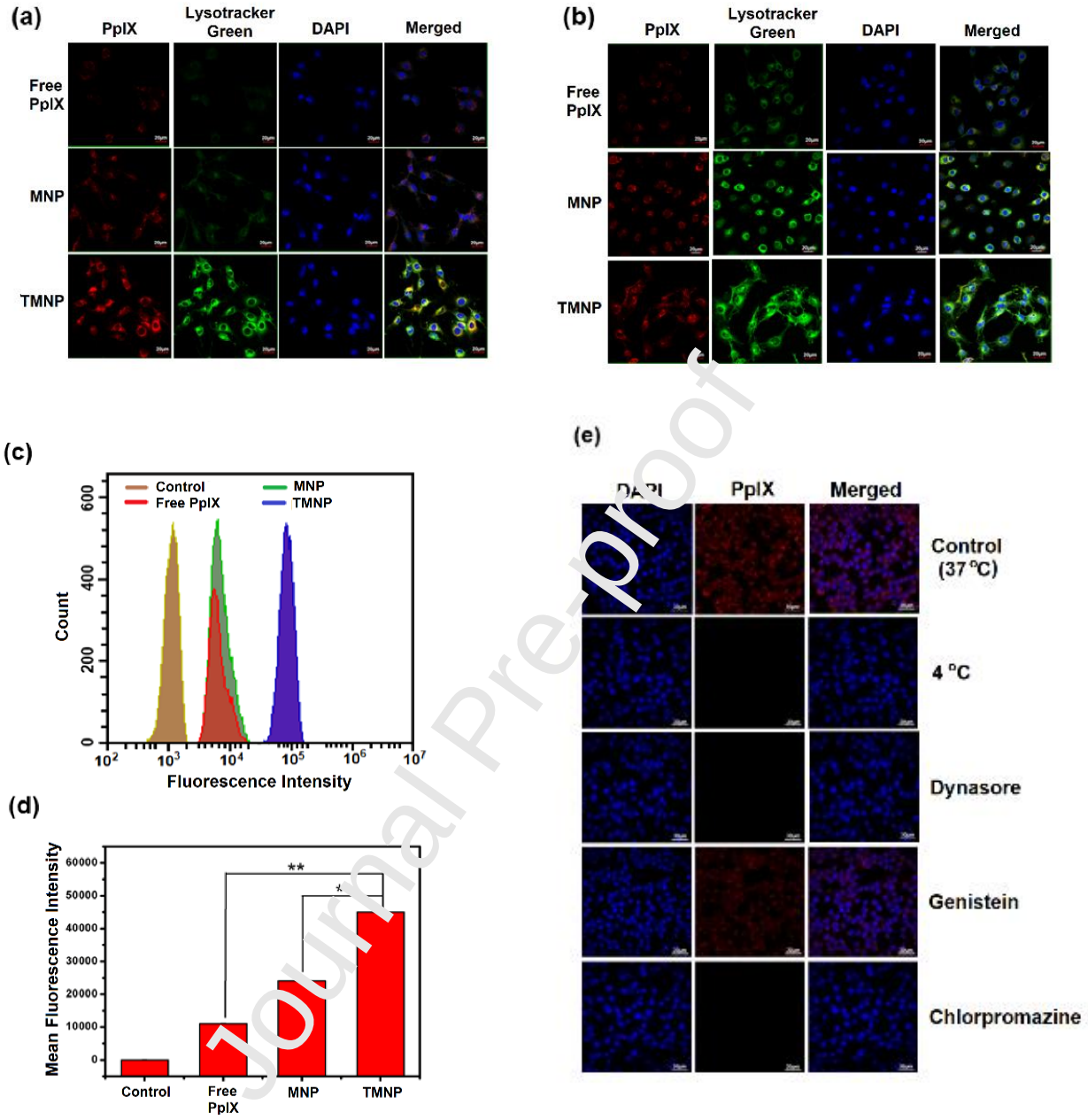

Figure 4. Cellular uptake dynamics. CLSM images showing the internalization and intracellular distribution of Free PpIX, MNP and TMNP in C6 cells at a) 3 hours and b) 6 hours. c) Quantitative analysis of the Free PpIX, MNP and TMNP uptake by C6 cells using flow cytometry. d) Mean fluorescence intensity of C6 cells after treatment with Free PpIX, MNP and TMNP. e) Cell uptake of TMNP after incubation at 37 °C and 4 °C and after preincubation with inhibitors of dynamin (dynasore) or caveolin (genistein) or clathrin (chlorpromazine). Scale bar, 20 μm. **P < 0.01 and ***P < 0.001.

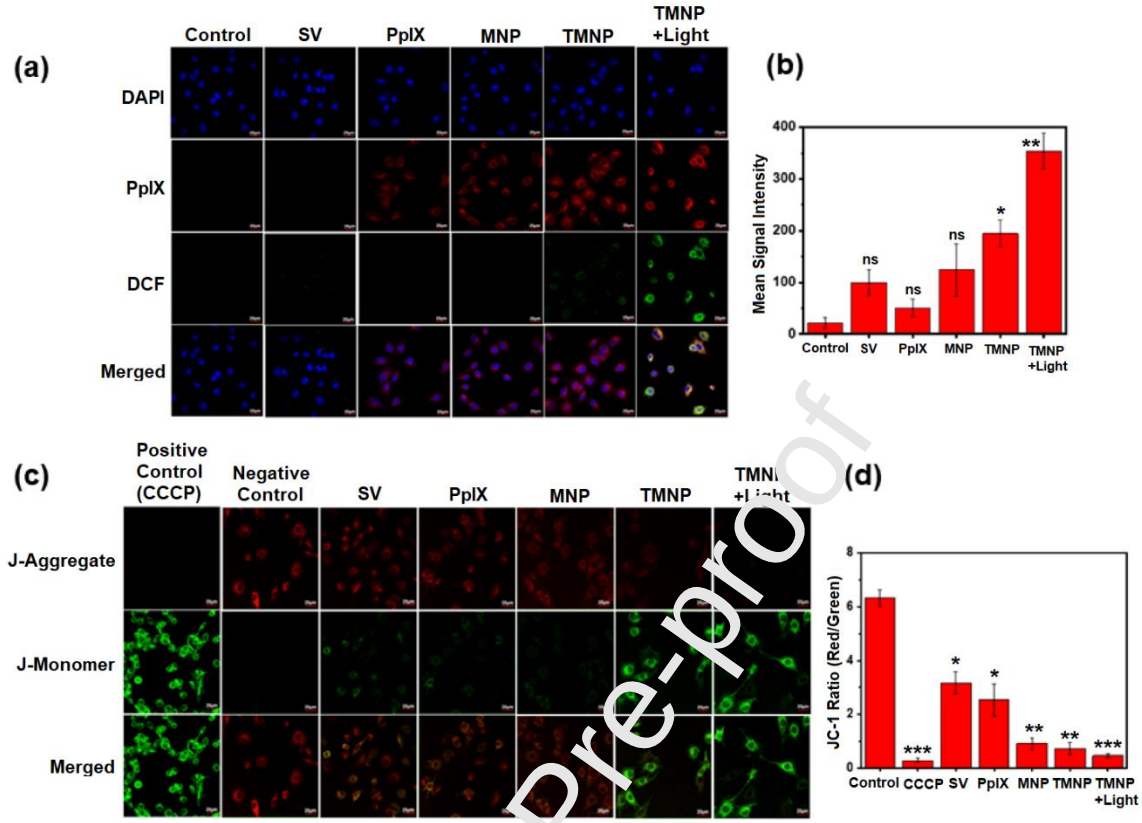

Figure 5. ROS generation assay: a) Cells were treated with different therapeutic agents and then exposed to a 635-nm laser (130 mW/cm^2 for 5 minutes). ROS generated in C6 cells was measured using DCFH-DA. CSLM images showing green fluorescence indicate positive staining for ROS. b) Quantitative analysis of ROS generation in cells treated with different agents and then exposed to a 635-nm laser (130mW/cm^2 for 5 minutes) detected using CellRox Green Reagent, JC 1 assay: c) CLSM images representing changes in mitochondria membrane potential when treated with different agents and then exposed to a 635-nm laser (130 mW/cm^2 for 5 minutes). d) Red-to-Green channel ratio of different agents determines the rate of membrane potential decay. *P < 0.05, **P < 0.01 and ***P < 0.001.

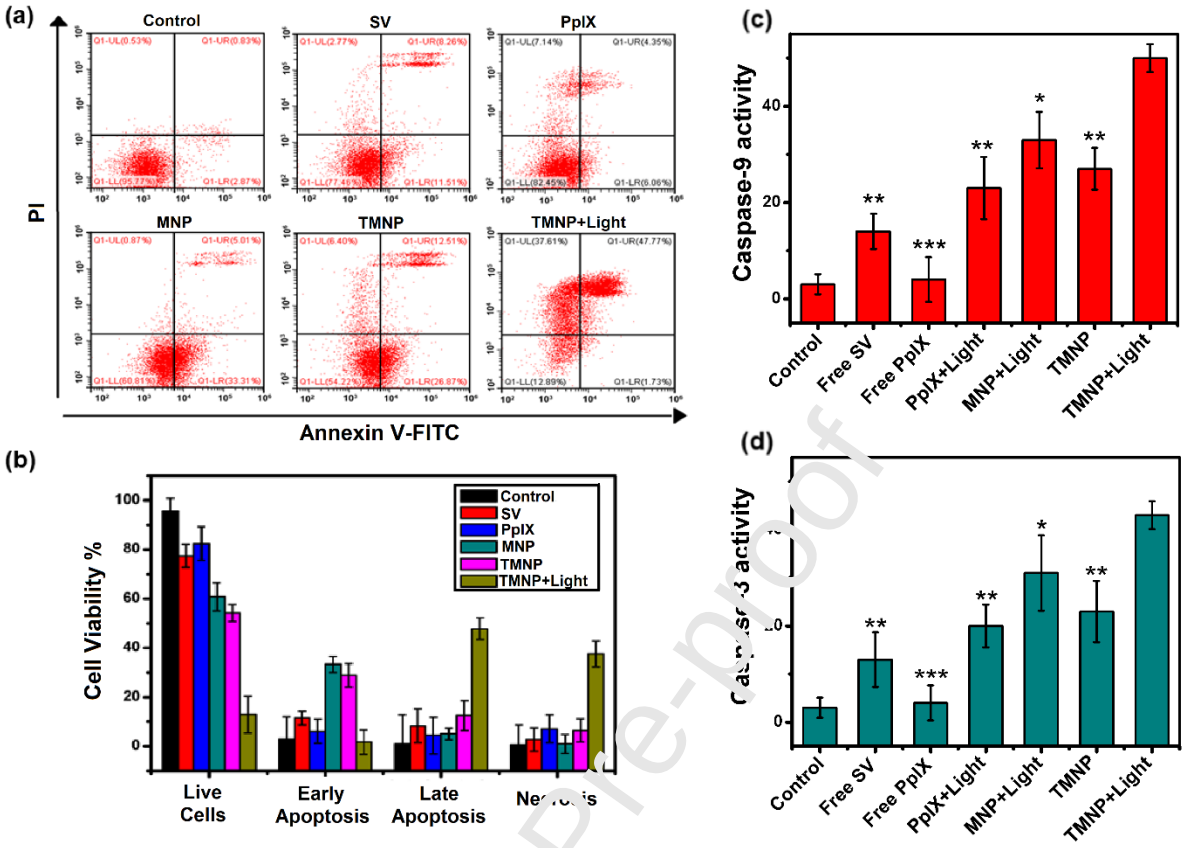

Figure 6. a) Annexin V/PI analysis of C6 cells incubated with DMEM (control), free SV, free PpIX, MNP, TMNP with/without irradiation (635nm laser at 130mW/cm^2 for 5 minutes). The quadrants from lower left to upper left (counter clockwise) represent healthy, early apoptotic, late apoptotic, and necrotic cells, respectively. (b) The percentage of cells in each quadrant was shown on the graphs. c) Caspase-9 activity and d) Caspase-3 activity after treatment with Free SV, Free PpIX, PpIX+Light, MNP+Light, TMNP and TMNP+Light. All the data values are presented as mean ± SD (n = 3). *P < 0.05, **P < 0.01 and ***P < 0.001.

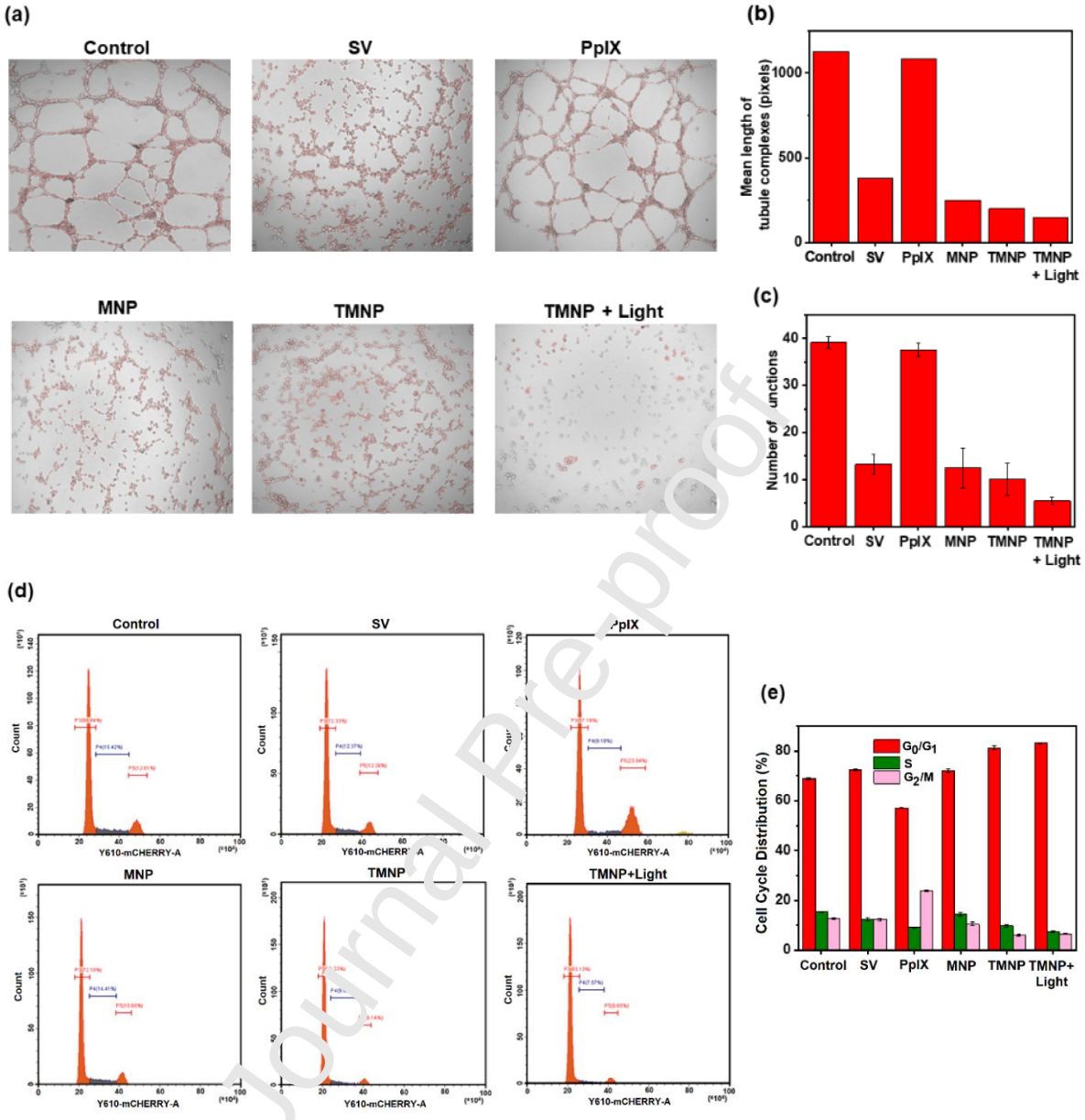

Figure 7. Angiogenesis assay on HUVEC cells: a) Phase contrast images show endothelial cells grown on matrigel after treatment with different agents. Results from computer assisted quantitative analysis of angiogenesis showing b) mean length of tubule complexes and c) number of junctions. Effect of different agents on cell cycle progression: d) The cell cycle distribution was determined by a flow cytometric analysis of the DNA content after staining with propidium iodide. e) Data expressed as mean ± SD from three independent experiments. *P < 0.05, **P < 0.01, ***P < 0.001 and ns – Not Significant.

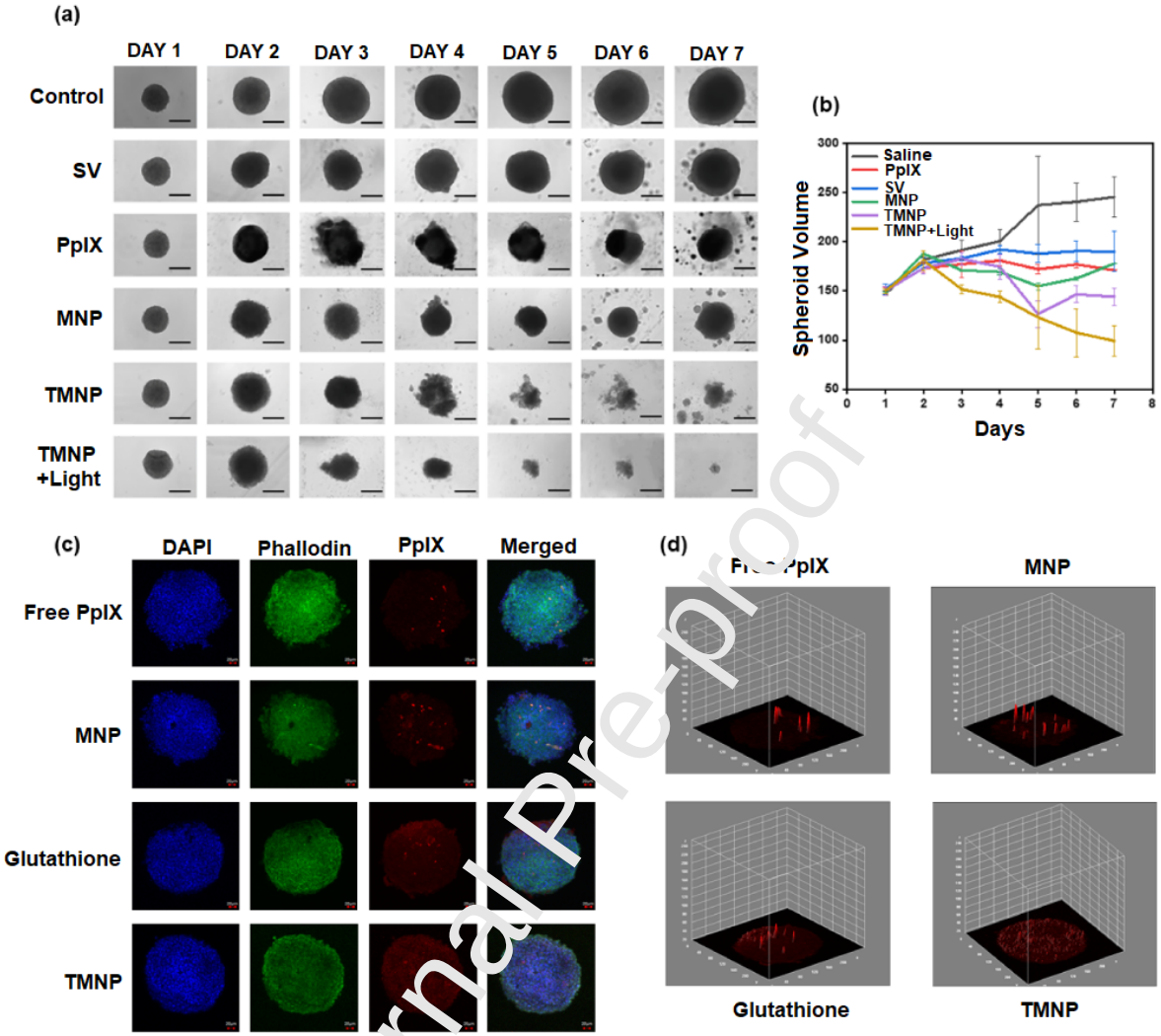

Figure 8. Growth Inhibition assay in C6 MCs: a) Sequential Bright-field images of the same C6 spheroids treated with free SV, free PpIX, MNP, TMNP, TMNP+light (Scale bar = 275µm), b) Volume changes of MCs over 7 days. Data represents average ± standard deviation of three (n=3) independent measurements. Penetration and Distribution in C6 spheroids: c) CLSM images of C6 MCs treated with Free PpIX, PpIX+Micelles, PpIX+T-Micelles and C6 MCs pre-incubated with Glutathione (1mg/ml) before treatment with PpIX+T-Micelles for 6 hours. Scale bar, 20 µm, d) Surface plots of images in (a), produced in Image J.

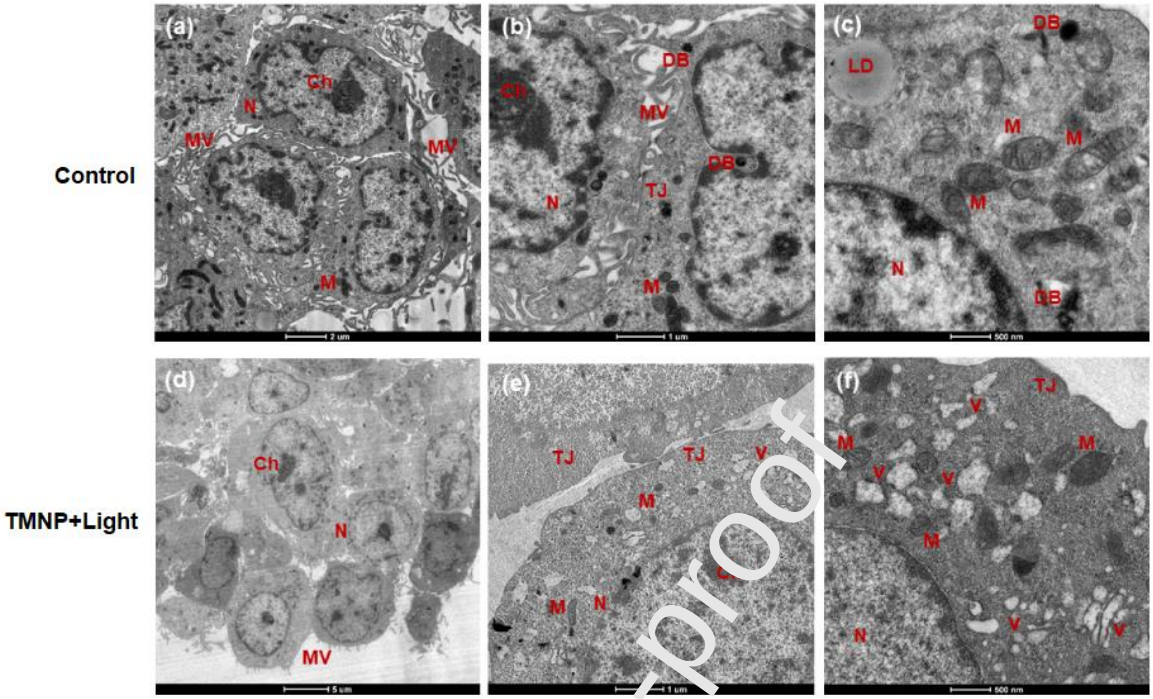

Figure 9. TEM image of C6 tumour spheroids after 36 h culturing (a, b and c) Control group (d, e and f) Spheroids treated with TMNP at a concentration of 0.093 µg/mL for 12 h. Ch: chromatin; DB: Dense body; LD: Lipid droplet; M: Mitochondria; MV: Microvillus; N: Nucleus; TJ: Tight junction; V: vacuole.

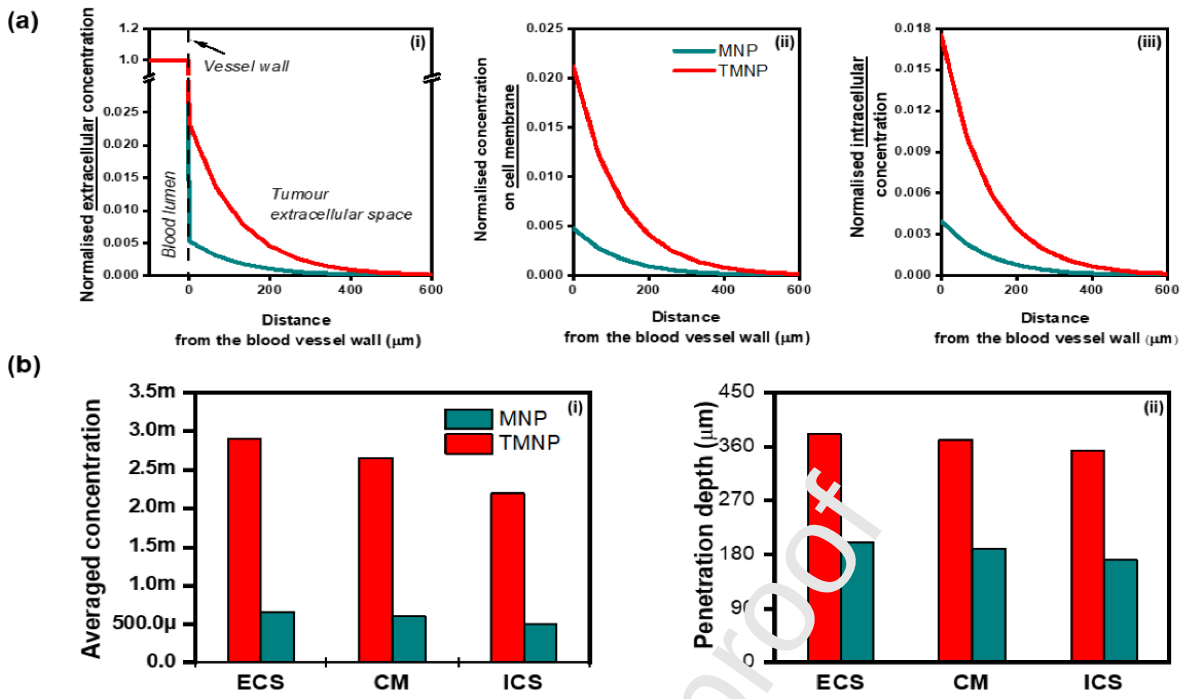

Figure 10. a) Comparison of TMNP and MNP concentration in each tissue compartment as a function of distance from blood vessel wall. Concentration i) in ECS, ii) on CM and iii) in ICS of tumour tissue, normalised by C_{IVS}. b) Comparison of TMNP and MNP delivery outcomes in each tissue compartiment. i) Spatial averaged concentration, which is normalised by C_{IVS}. ii) Penetration depth which is counted when the local concentration is greater than 0.1% of C_{IVS}.